# Three-dimensional crustal structure in the Southern Alps region of New Zealand from inversion of local earthquake and active source data

Donna Eberhart-Phillips

Institute of Geological and Nuclear Sciences, Dunedin, New Zealand

Stephen Bannister

Institute of Geological and Nuclear Sciences, Lower Hutt, New Zealand

[1]  *P* and *S-P* arrival time data from 311 earthquakes and several thousand offshore and onshore shots have been used in simultaneous inversion for hypocenters, three-dimensional (3-D) $Vp$ and $Vp/Vs$ models in the Southern Alps region, New Zealand. The combined data result in a highly nonuniform ray path distribution, and linked nodes are used in sparsely sampled areas. Gravity data are used to improve the model below 20-km depth, where it is poorly sampled by local earthquakes. The crustal $Vp$ from 5 to 25 km depth is fairly uniform, generally ranging from 5.5 to 6.5 km/s, typical of graywacke and schist. Active fault zones tend to be correlated with low-velocity zones. Where the Alpine fault is primarily strike slip, it is characterized by a vertical low-velocity zone, to at least 15-km depth. Where the fault is dipping and has a large dip-slip component, it is characterized by a large region of low velocity above and southeast of the fault, to at least 14-km depth, consistent with fluids and fracture density from active deformation. A large high-velocity, high-resistivity feature in the eastern Southern Alps may represent Mesozoic schist of higher metamorphic grade than its surroundings, which is relatively rigid and serves to both reduce deformation in the overlying basin and concentrate deformation in the adjoining low-velocity region. The imaged crustal root is deepest 80-km south of Mt. Cook and is asymmetric with a sharper gradient on the northwestern side. The approximate Moho shows regional variation, with 5–10 km thicker crust in Otago than Canterbury.    *INDEX TERMS*: 8010 Structural Geology: Fractures and faults; 8180 Tectonophysics: Evolution of the Earth: Tomography; 8102 Tectonophysics: Continental contractional orogenic belts; 7205 Seismology: Continental crust (1242); *KEYWORDS*: Southern Alps, Alpine fault, seismic tomography, gravity, crustal root

**Citation:**  Eberhart-Phillips, D., and S. Bannister, Three-dimensional crustal structure in the Southern Alps region of New Zealand from inversion of local earthquake and active source data, *J. Geophys. Res.*, *107*(B10), 2262, doi:10.1029/2001JB000567, 2002.

## 1.  Introduction

[2] The South Island of New Zealand is undergoing oblique continental collision, with slip on the Alpine fault and uplift of the Southern Alps. The character of deformation varies along strike, with the Alpine fault merging into the Marlborough fault system on the northeast and becoming a crustal fault in the overlying plate of the Fiordland subduction zone to the southwest. Deformation is also influenced by the varied geology throughout the region (summarized by *Mortimer et al.* [1999]). The rock to the east of the Alpine fault is primarily Torlesse graywacke (Figure 1), although there are a few localities with Cretaceous intrusives and Miocene volcanics. A large portion of the Torlesse terrane experienced metamorphism during Jurassic to Cretaceous collision, resulting in the Haast Schist. The schist overprint occurs across the region south of the Waitaki-Waihemo Fault zone (WWFZ) and in a narrow band along the Alpine fault (Figure 1). Schist is inferred to underlie much of the graywacke, and postmetamorphic faulting has emplaced some schist blocks within the graywacke.

[3] The geologically determined slip rates along the Alpine fault have been summarized by *Norris and Cooper* [2000], showing a relatively uniform strike-slip rate of 26 mm/yr, about 70% of plate motion. The dip slip rate is highly variable, from about 6 mm/yr in the north, to greater than 10 mm/yr in a relatively short central section, and decreasing to zero in the southwest (Figure 1). Models of Southern Alps deformation (Figure 2) suggest that the Pacific plate crust moves upward along the Alpine fault, the lower ductile crust forms a crustal root, and the mantle moves downward [*Norris et al.*, 1990; *Stern et al.*, 2000; *Pysklywec et al.*, 2002]. The brittle-ductile transition is estimated from the base of the seismogenic zone, which is
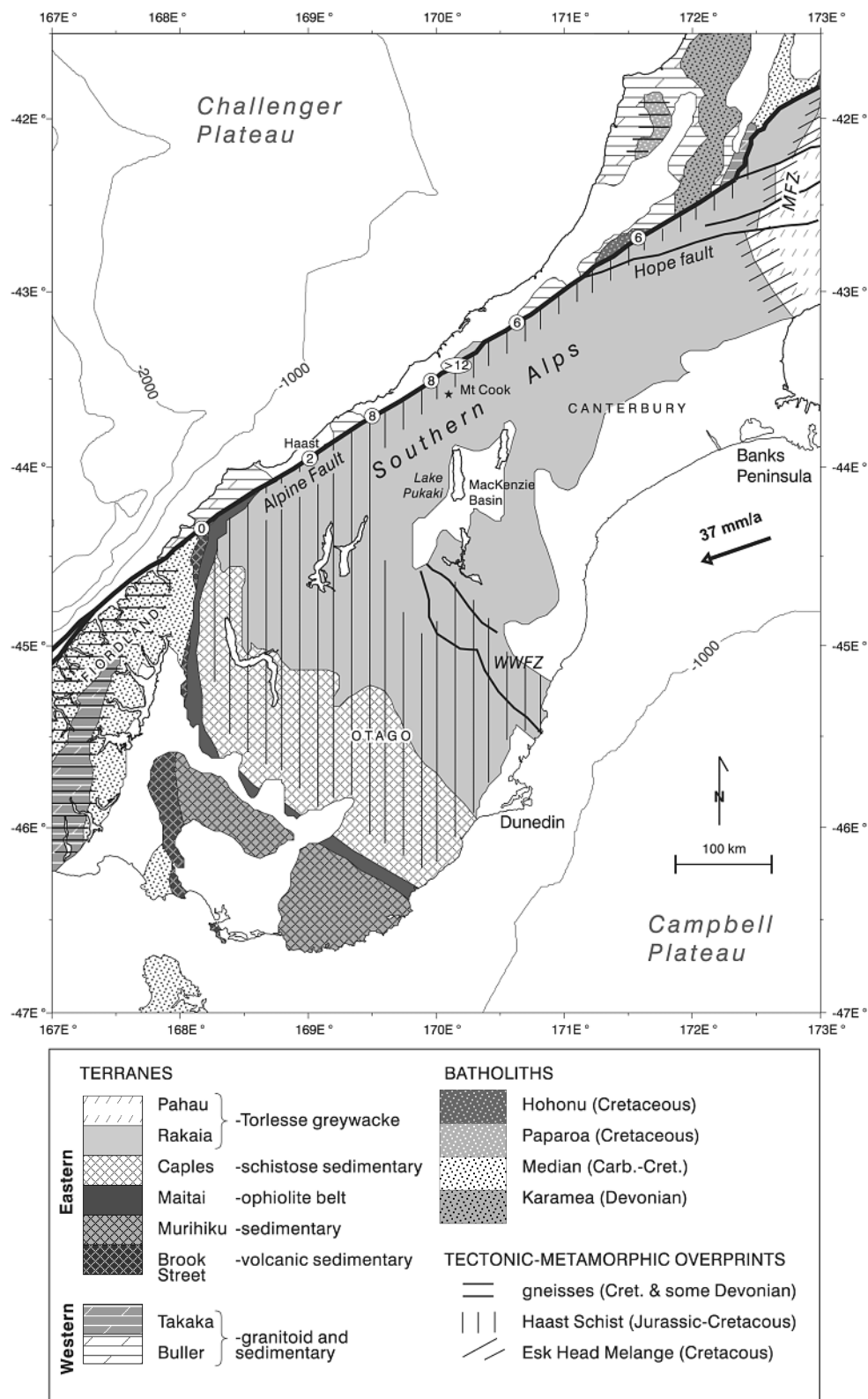
**Figure 1.** Tectonic setting of the South Island. Geologic terranes are after *Mortimer et al.* [1999]. Quaternary dip-slip rates at Alpine fault locations are indicated by circled numbers (mm/yr); strike-slip rate is uniformly 26 mm/yr [*Norris and Cooper*, 2000]. MFZ, Marlborough Fault Zone; WWFZ, Waitaki-Waihemo Fault Zone. Plate motion indicated by bold arrow; bathymetry in 1000-m contours.
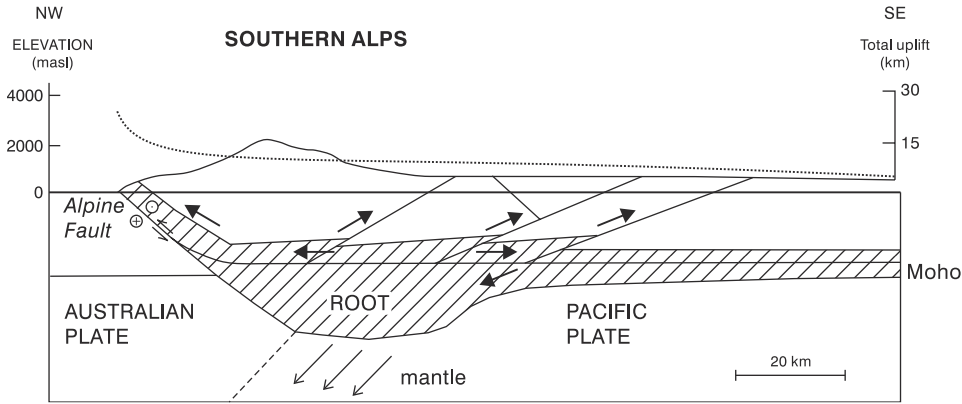
**Figure 2.** Schematic cross section through the Southern Alps (reprinted from *Norris et al.* [1990] with permission from Elsevier Science). Note that the Alpine fault has oblique slip accommodating about 70% of plate motion and the Southern Alps are eroding rapidly on the northwest side.

about $12 \pm 2$ km depth throughout the region [*Leitner et al.*, 2001].

[4] Geodetic measurements and analyses in the South Island show deep slip rates of about $21-36$ mm/yr strike slip and $11-18$ mm/yr dip slip below a locking depth of about 8 km, as well as slight variations in the strain pattern throughout the region [*Beavan et al.*, 1999; *Beavan and Haines*, 2001]. The geodetic slip rates are higher than Alpine fault paleoseismic rates because there are additional active deformation structures. Numerical modeling has shown the importance of rheological variations. *Gerbault and Davey* [2002] show that the 3-D shape of the crustal root can be explained by reduced strength in the Torlesse lower crust relative to both the Australian plate and southern South Island terranes. *Koons et al.* [1999] infer that the southern broadening of the active deformation zone is related to the inherited thicker crust south of the Waihemo fault zone, which is mechanically weaker.

[5] Imaging the 3-D velocity structure of the Southern Alps region is important for understanding crustal structure and its evolution, the influence of rheology on strain, and discerning factors that effect faulting. Our study combines passive and active seismic observations in the South Island to obtain the best fitting 3-D velocity structure. The 3-D model is complementary to other 2-D studies.

[6] The South Island Geophysical Transect (SIGHT) [*Stern et al.*, 1997; *Davey et al.*, 1998] was an integrated onshore and onshore-offshore seismic refraction and wide-angle reflection experiment, carried out across the South Island and extending about 200 km offshore both east and west of the South Island. The measurements were concentrated on two main profiles, while a third transect was completed along the southeastern margin of the South Island. SIGHT had three main components. The first stage involved wide-angle reflection/refraction along two land transects, T1 (north) and T2 (south), using 23 chemical explosions spaced equally across the South Island, and 420 recording instruments at a nominal spacing of 400 m (Figure 3). The second stage of SIGHT involved three offshore-onshore transects, offshore each end of T1 and
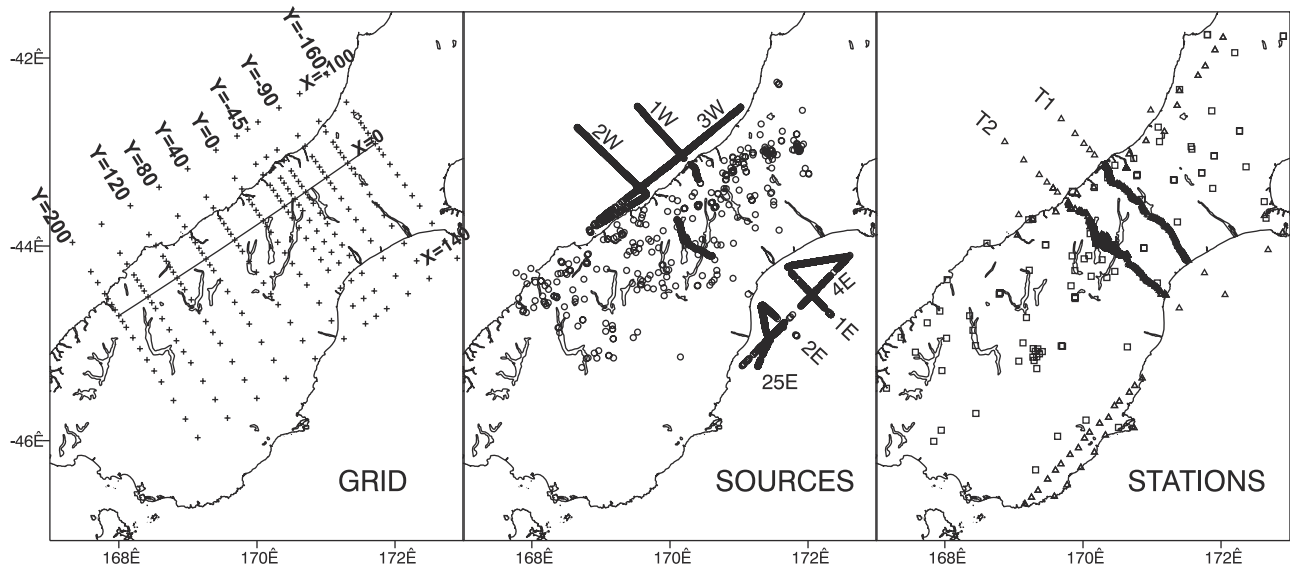


**Figure 3.** Sources and stations used in the data inversion, together with the nodes of the velocity grid. Note that peripheral nodes are also assigned at $y$ and $x = \pm 750$, so that the velocity is defined everywhere. Triangles are SIGHT stations; squares are SAPSE and other passive seismic stations.

T2, and also along east and west coast-parallel transects. Air gun shots continued even during the ship transition between the profiles and these were used for our 3-D model. OBH and OBS receivers were deployed on both sides of the South Island and these recorded the air gun shots.

[7] The third stage of SIGHT, carried out in 1998, two years after the onshore-offshore work, involved acquisition of deep multichannel seismic lines on the east (Mt. Cook) and west side of the Southern Alps. The chemical explosion shots were also recorded by several piggyback recording arrays, which were placed in critical locations. Separately, the Lake Pukaki seismic line [*Kleffmann et al.*, 1998] involved recording multichannel seismic data along a 27 km profile on the eastern margin of Lake Pukaki, with supplementary data recorded by a 52-km-long portable array spread over a line partially coincident with the reflection profile, and by permanent stations of the New Zealand National Seismograph Network (NZNSN).

[8] SIGHT data show eastward dipping reflectors below 20-km depth that coincide with the projected Alpine fault [*Stern et al.*, 1997]. Old (Cretaceous) oceanic crust below the graywacke is indicated by extremely strong lower-crustal reflections, but its thickness is quite nonuniform [*Stern et al.*, 1997; *Mortimer et al.*, 2002]. Models of wide-angle seismic data on T2 indicate low velocity to 30-km depth in the vicinity of the Alpine fault [*Davey et al.*, 1998; *Stern et al.*, 2001]. Low-fold stacks of T1 and T2 image an approximately 8-km-thick crustal root below the Southern Alps [*Davey et al.*, 1998; *Okaya et al.*, 2002]. Combined onshore-offshore transect data have been used to form profiles out to undeformed parts of the Australian and Pacific plates. These profiles include details of shallow offshore basins and thinning of the Australian crust near the edge of the Challenger Plateau [*Okaya et al.*, 2002; *Scherwath et al.*, 2000; *Van Avendonk et al.*, 1999].

[9] The Southern Alps Passive Seismic Experiment (SAPSE) [*Anderson et al.*, 1997] contained stations distributed throughout the South Island to record both active and passive source data. The array consisted of 26 broadband and 15 short-period temporary seismometer stations, augmenting 17 permanent NZNSN seismometer stations. The stations were broadly distributed, but centrally weighted to the central Alpine Fault and the regions near the active-source-transects (Figure 3). Seismicity recorded by SAPSE has been analyzed by *Leitner et al.* [2001]. Estimates of variations in crustal thickness have been obtained from binned stacked earthquake data [*Wilson and Eberhart-Phillips*, 1998] and receiver functions [*Parker*, 1999].

[10] *Wannamaker et al.* [2002] obtained 41 magnetotelluric soundings across the Southern Alps region close to seismic transect T1, to probe deep thermal and fluid states beneath the South Island. Their primary inferred structure from inversion models of the data is a conductive zone in the middle to lowermost crust extending about 15–35 km in depth. They model the conductive feature as a fluidized zone in the deep crust (with possibly a quite small fluid content <0.5%) due to prograde metamorphism related to crustal thickening. Fluids are interpreted to rise toward and above the Alpine fault and are linked with recent mesothermal veining and gold deposition. Fluids are also inferred to rise toward the back-thrust Forest Creek fault zone, which is supported by O and C isotopic evidence [*Upton et al.*, 2000].

## 2.  Data

[11] Figure 3 shows the seismic sources and receiver stations used for the velocity inversion, together with the nodes of the velocity grid used in the model parameterization and velocity inversion. The passive source data comprise 5709 *P* arrivals and 1650 *S* arrivals from earthquakes. These earthquakes were recorded by either SAPSE stations [*Anderson et al.*, 1997] between 1995 and 1997, the SIGHT transect stations [*Stern et al.*, 1997] during 1996, or by the Pukaki array [*Reyners*, 1987] between 1975 and 1983. The few earthquakes deeper than 25 km were selected from the Pukaki array and they provide ray paths which are deeper than many of the ray paths obtained from the active source data. Good *P* wave arrival times were picked with a typical accuracy of 0.03 s, and *S* arrivals with an accuracy of 0.1 s. Accuracy varies because of varied signal-to-noise ratio and because scattered and converted energy can reduce the certainty in selecting an arrival as the true *P* or *S* arrival. Observation qualities assigned by the seismic analysts are used to weight the data.

[12] Active source data, comprised of 35,152 *P* arrivals, were recorded during the 1996 SIGHT offshore-onshore experiment and the 1998 SIGHT multichannel seismic survey. The transects and air gun profiles are shown in Figure 3. In addition to the 1996 SIGHT in-line, offshore-onshore transect data, the active source data set also includes air gun data with ray paths which are quite oblique to the SIGHT transect lines. These oblique ray paths provide increased 3-D sampling of the crustal structure. In particular we use *P* wave arrivals from air guns on offshore lines 2W, 3W, 4E, and 25E which were recorded on the onshore transect lines. In addition, the same air gun shots were well recorded by the distributed broadband SAPSE stations and by offshore OBH and OBS receivers. The low attenuation of the crust enabled signals from the active sources to be discernible for up to 300 km. Travel times from all air gun sources were reduced to a seafloor datum, using known bathymetry. *P* wave arrival times were picked with a typical accuracy of 0.01s.

[13] *P* wave arrivals were also recorded from 23 onshore explosive shots, which were spaced across the South Island about 10-km apart on the northern transect (T1) and about 22 km apart on the southern transect (T2) [*Stern et al.*, 1997]. In addition the active source data also include arrivals recorded during the 1998 SIGHT survey, which involved higher-resolution multichannel deep seismic lines on both the west and east sides of the Southern Alps, as well as several smaller localized piggyback deployments.

## 3.  Method

[14] Arrival times of local earthquakes and shots were used in a simultaneous inversion for hypocenters and three-dimensional (3-D) *P* velocity and $Vp/Vs$ ratio [*Thurber*, 1983, 1993; *Eberhart-Phillips*, 1990, 1993; *Eberhart-Phillips and Michael*, 1998]. Seismic methods do not measure a bulk volume but rather measure material properties along the seismic propagation path from the source to the receiver.

The source locations are also unknown with earthquake data. Hence consideration must be given during the inversion procedure to obtaining a reasonable velocity model from the nonuniform sampling of the 3-D volume. We desire a crustal model that is useful for other applications such as defining 3-D rheology in numerical deformation models so we aim for a reasonable model even in areas where we have little seismic resolution. The travel time $t_{ij}$ residual $r_{ij}$ for event $i$ and station $j$ is related to small changes in hypocentral ($x$, $y$, $z$, and ot (origin time)) and velocity $v$ parameters as

$$r_{ij} = \Delta \text{ot}_i + \frac{\partial t_{ij}}{\partial x_i} \Delta x_i + \frac{\partial t_{ij}}{\partial y_i} \Delta y_i + \frac{\partial t_{ij}}{\partial z_i} \Delta z_i + \sum_{n=1}^{N} \frac{\partial t_{ij}}{\partial v_n} \Delta v_n.$$

The velocity of the medium is parameterized by assigning velocity values at the intersections (nodes) of a 3-D grid. Hypocentral coordinates are fixed for shots. The ray paths are calculated with an approximate 3-D ray-tracing algorithm that produces curved nonplanar ray paths which are defined by points more finely spaced than the velocity nodes. Since the ray paths and hypocenters depend on the velocity, the partial derivatives are approximate, and nonlinearity requires an iterative solution to obtain reliable model parameters. The solution is obtained by iterative, damped least squares, without additional smoothing,

$$\Delta \mathbf{m} = \{\mathbf{M}^{\mathrm{T}} \mathbf{M} + \theta^2 \ \mathbf{I}\}^{-1} \ \mathbf{M}^{\mathrm{T}} \mathbf{r}',$$

where $\mathbf{m}$ is the vector of medium parameters, $\mathbf{M}$ is the matrix of medium partial derivatives transformed by parameter separation of the hypocenter parameters, $\theta^2$ is the damping, and $\mathbf{r}'$ is the transformed vector of residuals [*Thurber*, 1983]. For each iteration, new ray paths are determined, the hypocenter solution is included, and parameter separation is carried out. The full resolution matrix is also calculated.

[15] Damping leads to a conservative solution that fits the data well with few artifacts. The appropriate damping is selected with a trade-off analysis of data variance and model variance to obtain a damping parameter which greatly reduces data variance with moderate increases in model variance [*Eberhart-Phillips*, 1986]. For example, solutions with low and appropriate damping are compared in Figures 4b and 4d. The data variance is only 1% less with lower damping, but the model variance is 28% greater. The patterns of velocity heterogeneity are similar, but there are some possible artifacts in the low-damping solution, such as single node anomalies, minor velocity reversals, and large velocity perturbations below 40-km depth. If there is uneven data distribution, some areas in a damped least squares inversion will be unperturbed because they do not have enough information. In global tomography with block parameterization, *Bijwaard et al.* [1998] have thus obtained improved solutions by using larger block sizes in areas where there are fewer ray paths. For the grid parameterization, we can link together nodes to vary the volume size associated with inversion solution parameters.

[16] Throughout the inversion, weighting is applied to each observation, based on the observation quality assigned by the seismic data analyst, the source-receiver distance, and the size of residual. The residual downweighting deals with data that is inappropriate due to such factors as incorrect station timing or wrong arrivals picked. The limits are set high so that observations with residuals greater than 1.5 s are significantly downweighted and only residuals greater than 2.75 s are discarded, while residuals from 0.5 s to 1.5 s are slightly downweighted. This procedure means that very little data are actually thrown out, and it usually leads to less and less data being downweighted as the iterative inversion proceeds and the solution fits the data better. There will of course be some residuals that reflect localized small-scale velocity heterogeneity which cannot be fit by the relatively coarse grid spacing. Out of 40,861 observations, only 114 were discarded and 320 were significantly downweighted. These observations had bad residuals regardless of the initial model.

[17] We used a grid that is oriented N56°E, parallel to the major structural feature, the Alpine fault, with the grid origin at the SAPSE Mt. Cook Village station (Figure 3). We used an initial velocity model that had an approximate 3-D Moho based on the results from the 2-D transects and other seismic studies. Active source velocity models provide 2-D variation in crustal structure along T1 and T2 [*Kleffmann*, 1999; *Scherwath et al.*, 2000; *Van Avendonk et al.*, 1999], as they use reflected arrivals from the Moho. Additional information for the initial velocity model was provided by velocity modeling on transect 3 [*Godfrey et al.*, 2001], and line 3W (A. Melhuish, personal communication, 1998). Away from the SIGHT transects there is information on broad crustal thickness variations from analysis of *PmP* arrivals [*Wilson and Eberhart-Phillips*, 1998]. Comparison between solutions with our 1-D and 3-D initial models (Figures 4a and 4d) shows that the same features are imaged in the well-resolved area above 20-km depth, but there are some misplaced features in the 1-D initial model solution, such as higher velocity on the east at 14-km depth where there should be a shallower Moho (as included in the 3-D initial model). The 3-D initial model solution also fits the data better, with a 13% lower data variance than for the 1-D initial model solution.

[18] Linked nodes [*Thurber and Eberhart-Phillips*, 1999] are used where there is less resolution. Several velocity nodes can be linked to one solution parameter for velocity perturbation. An area of linked nodes may have the same velocity perturbation, but need not have uniform velocity since the initial model may have a velocity gradient. Decisions on which nodes to link can be made manually on the basis of spatial patterns in geology, or automatically. We use the derivative weighted sum (DWS) to guide linking. Since the DWS is computed for all nodes prior to the inversion, it can be evaluated for a larger number of nodes than is feasible for inversion. We linked nodes that had DWS less than 10% of the DWS of the well-resolved nodes, but we did not link nodes over large regions unlikely to actually have uniform velocity perturbation.

[19] For $Vp$, most of the nodes in the central area to 22-km depth had adequate DWS. We manually linked other low DWS nodes to adjoining nodes horizontally or vertically. The largest linked areas were offshore areas that were very sparsely sampled but away from the primary plate boundary structures. $Vp/Vs$ was poorly sampled overall because no active-source $S$ wave data was picked, many
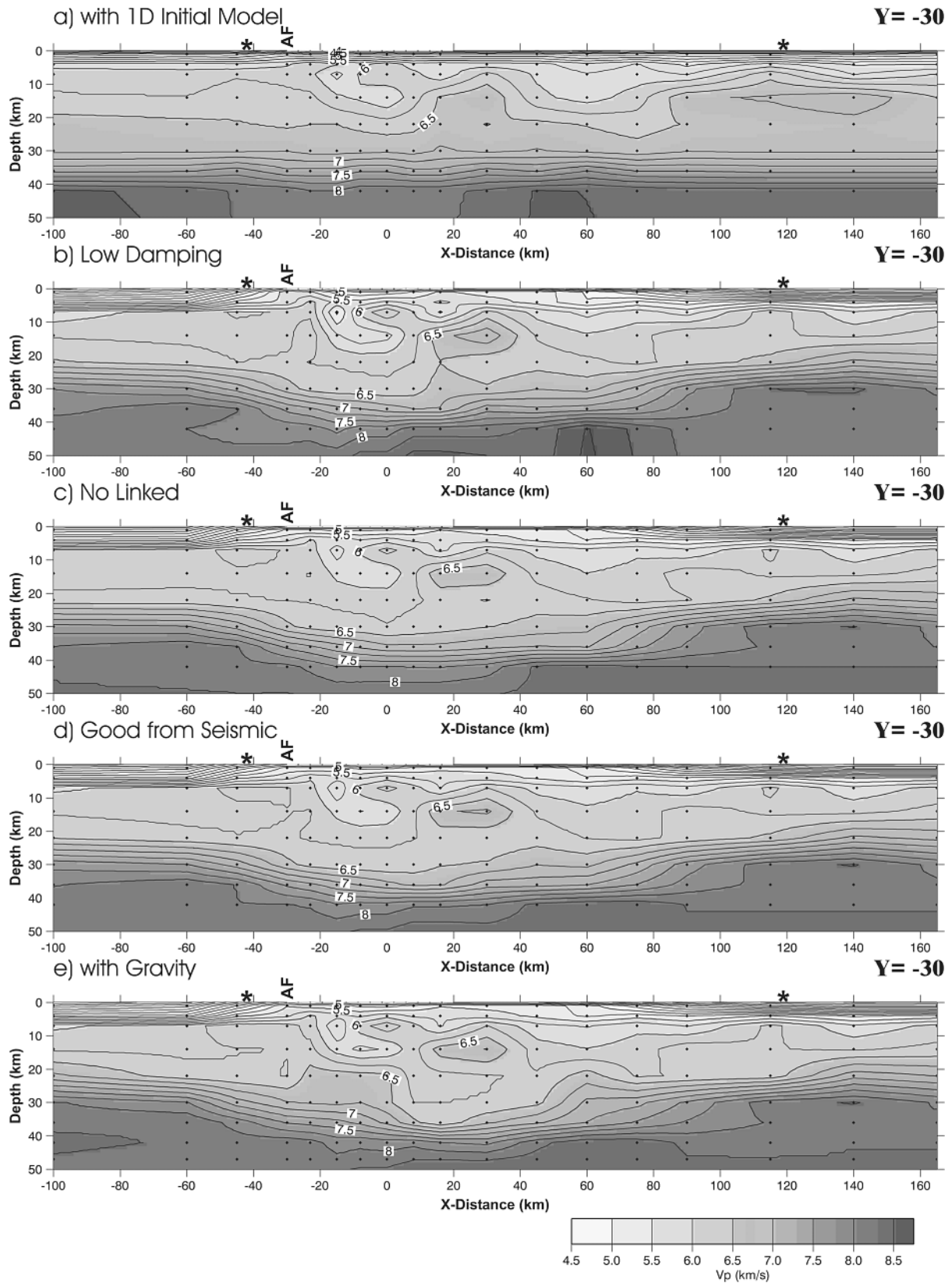
**Figure 4.** Comparison of various inversions, along $y = -30$ cross section. Stars at the top of sections denote the coastline, Alpine fault (AF) is indicated. (a) Using 1-D initial model. (b) Using low damping. (c) No linked nodes included. (d) Inversion of seismic data with appropriate damping, linked nodes, and 3-D initial model. (e) Including additional perturbations below 20-km depth using gravity data.
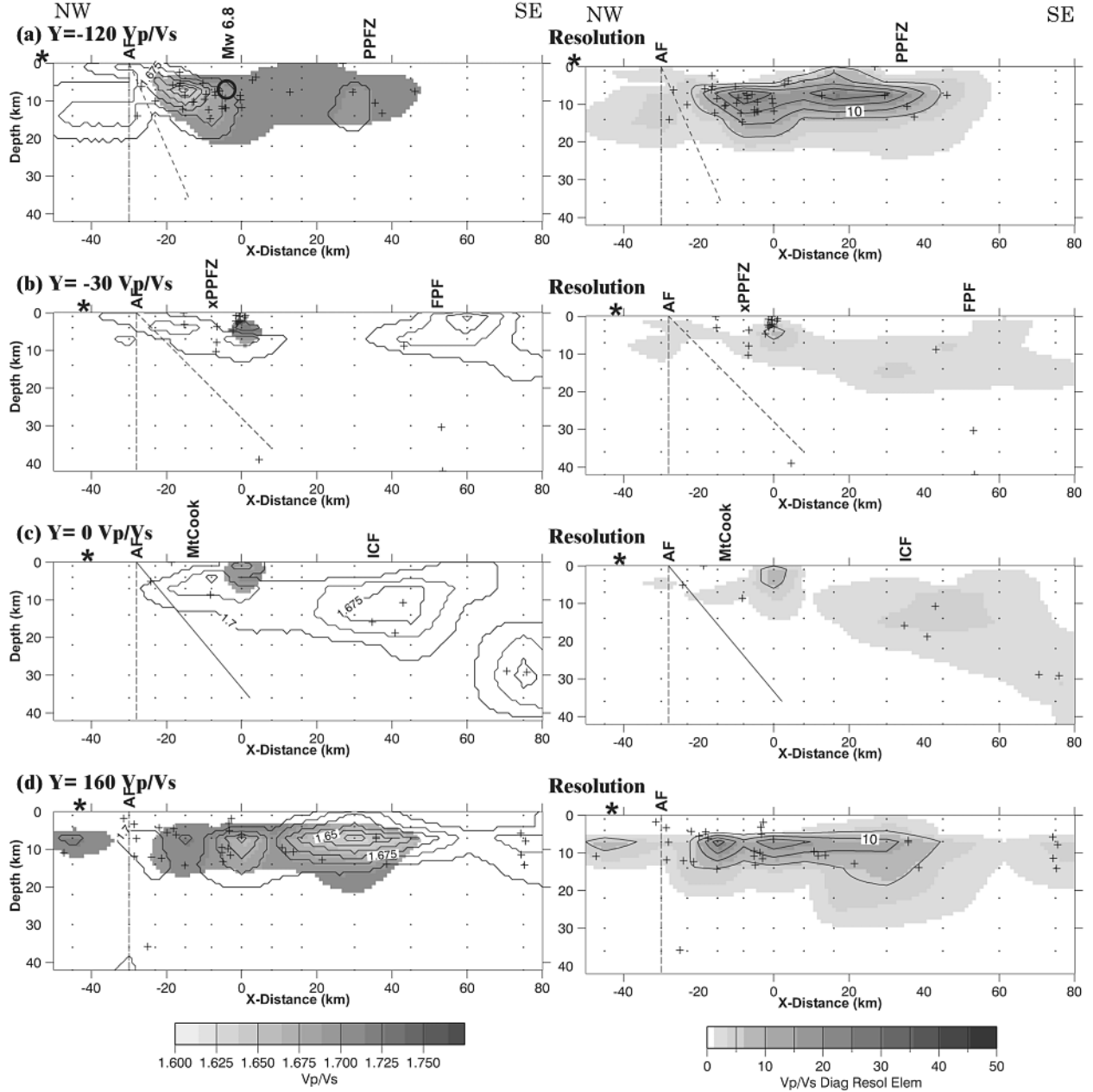
**Figure 5.** (left) Y cross sections of no-linked-nodes $Vp/Vs$ model, $y = -120$, $-30$, $0$, $160$, and (right) resolution from diagonal resolution element. Areas with low resolution (DRE < 5) are masked but contoured. Each section shows hypocenters (pluses) midway to next section. Small dots indicate velocity nodes. Stars at the top of sections denote the coastline. Dip of Alpine fault is not known, so both vertical and dipping lines are shown. Locations are indicated for: the Alpine fault (AF), Porters Pass fault zone (PPFZ) and incipient PPFZ (xPPFZ), Fox Peak fault (FPF), Irishman's Creek fault (ICF). Circles show significant earthquakes.

stations were vertical component only, and $S$ arrivals are generally more difficult to pick. Thus the $Vp/Vs$ linking was automated with a routine that linked up to 12 nodes together. In a handful of cases the autolinked $Vp/Vs$ nodes were separated when they included areas with known differences in lithology or $Vp$.

[20] The linked nodes inversion velocity model is similar to models without linking and has a 15% lower data variance. This improvement is not due to reducing the number of parameters, but to having more significant velocity perturbations in sparsely sampled areas. All the same $Vp$ features are present in the nonlinked solution (compare Figures 4c and 4d), but velocity perturbations below 20-km depth tend to be larger in the linked solution. The nonlinked $Vp/Vs$ solution has only sparse patches of perturbation where there are nodes with substantial resolution (Figure 5). The linked-nodes solution has $Vp/Vs$ defined over larger areas, both horizontally and vertically
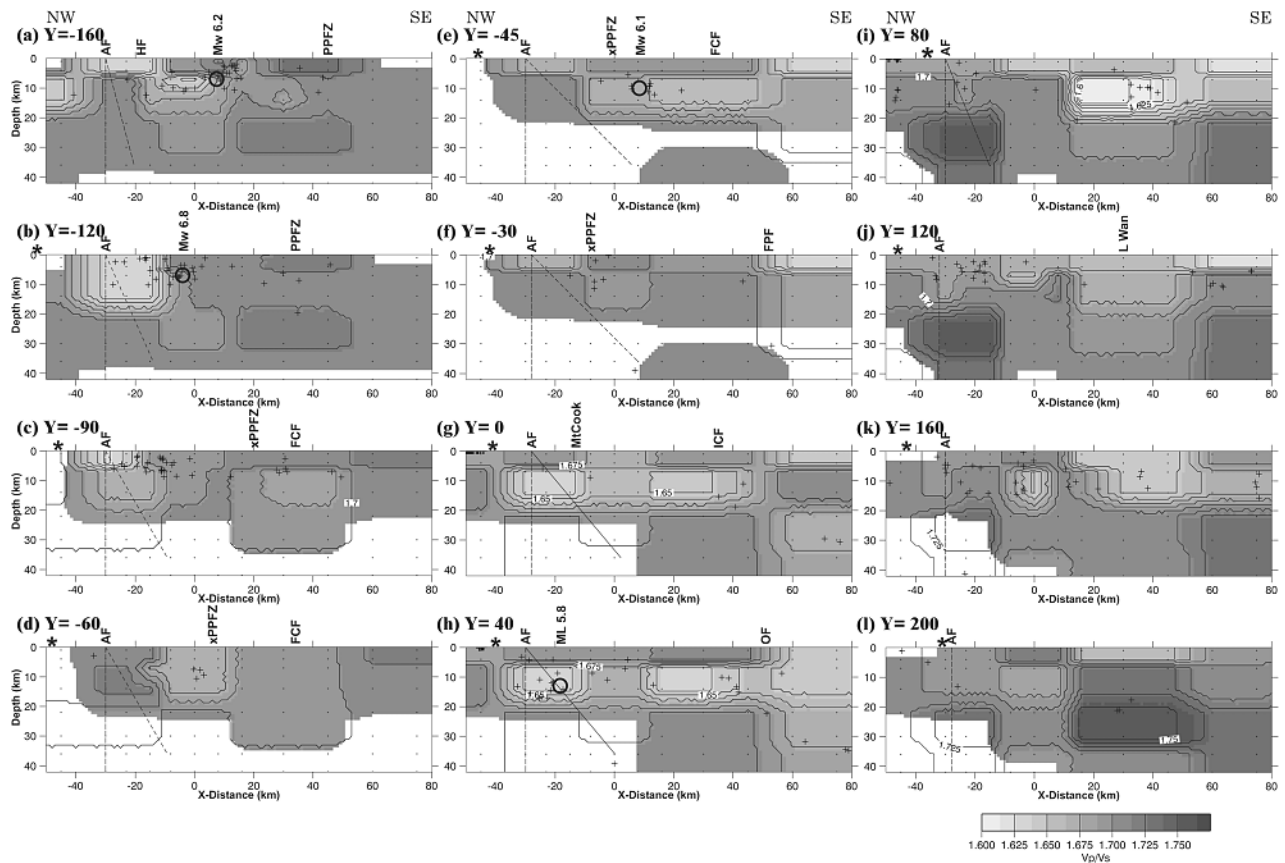
**Figure 6.** Y cross sections of *Vp/Vs* model with linked nodes. Areas with low resolution (DRE < 5) are masked but contoured. Each section shows hypocenters (pluses) midway to next section. Small dots indicate velocity nodes. Stars at the top of sections denote the coastline. Dip of Alpine fault is not known, so both vertical and dipping lines are shown. Locations are indicated for: the Alpine fault (AF), Hope fault (HF), Porters Pass fault zone (PPFZ) and incipient PPFZ (xPPFZ), Forest Creek fault (FCF), Fox Peak fault (FPF), Mt. Cook, Irishman's Creek fault (ICF), Ostler fault (OF), Lake Wanaka. Circles show significant earthquakes.

(Figure 6), which fits the data better and is easier to interpret than the few isolated patches in the nonlinked solution. Thus the solution is improved by allowing a finer grid for *Vp* in the central area than is justified for *Vp/Vs* or for peripheral areas.

[21] From the travel time data, we have little resolution below 20-km depth, yet there should be significant velocity and density variations below 20-km depth in the Southern Alps crustal root. The long-wavelength gravity low observed over the central South Island results from variations in crustal thickness of up to 15 km [*Woodward*, 1979]. Therefore gravity can be used in a secondary inversion to improve the deeper part of the 3-D Vp model, with gravity residuals related to velocity perturbations [*Eberhart-Phillips*, 1993] using an empirical velocity-density relationship [*Gardner et al.*, 1974; *Hill*, 1978]. Using Bouguer gravity upward continued 10 km, with 2-km *x*-grid spacing and 4-km *y*-grid spacing, we invert for *Vp* perturbations from 22 to 42 km depth, with minimum allowable *Vp* of 6.25 km/s and maximum allowable *Vp* of 8.35 km/s. The gravity is upward continued since we are not solving for shallow features. In order to have a final model that both fits the gravity and earthquake data, the 3-D model from the gravity inversion was then input into another iteration of the travel time inversion, which produced only minor velocity perturbations. The travel time only model and the model including gravity are compared in Figures 4d and 4e.

[22] The final model has a 90% reduction in gravity data variance from the travel time only 3-D model. The model with improved deeper structure is also useful for the travel time data, and the resultant final 3-D *Vp* and *Vp/Vs* models fit the travel time data slightly better than the model without improved deeper structure. The final model has an overall 56% reduction in travel time data variance from the initial model.

[23] The observed and calculated gravity are compared in Figure 7. The patterns and gravity gradients are very similar. We do not expect to obtain an ideal fit since we are only trying to improve the deep structure, and the general velocity-density relationship will not be correct for all rock types. There may be rocks that have similar velocity but different density, and characteristics such as high fluid
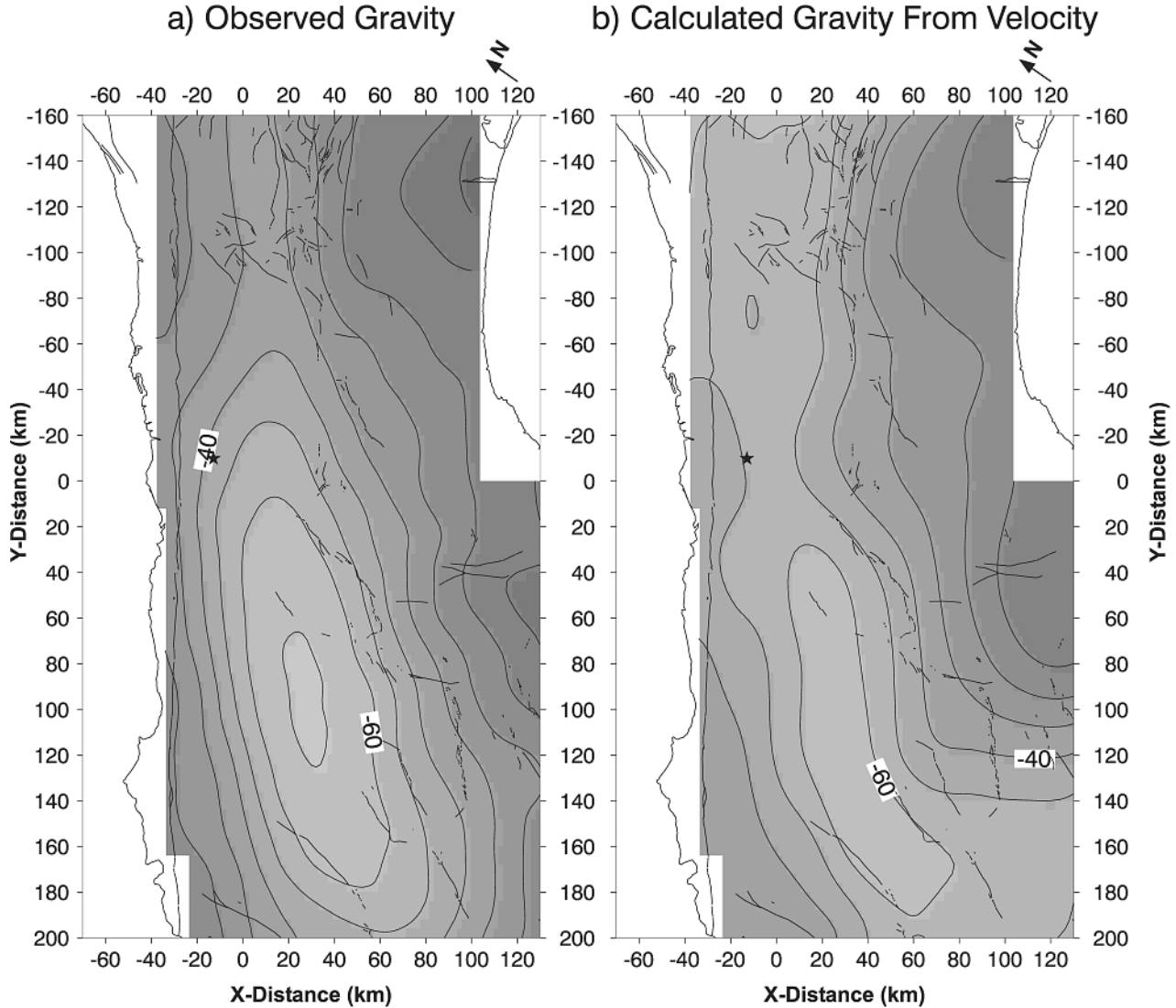
## a) Observed Gravity

## b) Calculated Gravity From Velocity



**Figure 7.** Comparison of gravity observed and calculated. (a) Bouguer gravity, upward continued 10 km, 2-km *x*-grid spacing, 4-km *y*-grid spacing. (b) Calculated from 3-D velocity model, obtained by combined gravity and travel time inversion. Contour interval is 10 mGal; star indicates Mt. Cook.

pressure will decrease velocity but have negligible effect on density. Also, while the crustal structure is reasonable in the 3-D model, the features may have slightly different shapes than in the velocity model where the shape is affected by the velocity grid and the resolution.

## 4. Results

[24] The *P* velocity is shown as cross sections in Figure 8. Inversion hypocenters and other significant earthquakes are shown. The dip of the Alpine fault varies and is not precisely known, but geologists estimate it to be around 45° in the central section where it has the most dip slip, and near vertical in the southern section where it is purely strike slip [*Norris and Cooper*, 2000]. Hence both vertical and dipping lines are drawn on the cross sections.

[25] The resolution pattern is shown by the computed diagonal resolution elements (DRE) (Figures 9 and 10). Since each set of linked nodes is treated as a single

parameter in the inversion, all nodes in each set are shown with the resolution of that parameter. The resolution matrix accurately shows the pattern of data distribution and spatial averaging; however, the damping factor reduces all the values of the resolution so that the DREs may be much less than the 1.0 values anticipated without damping [*Toomey and Foulger*, 1989]. For the Southern Alps inversion, the resolution is good in most of the central region from 5 to 20 km depth, with DREs of 0.1–0.4. In a low-damping inversion (Figure 4b), the DREs are much higher, 0.2–0.7, but the increased model variance is not justified by the marginal reduction in data variance. The calculated standard errors for nodal velocities computed in the inversion for velocities are 0.01–0.03 km/s. For an inversion with low damping, the standard errors are 0.02–0.09 km/s. *Thurber* [1981], in tests with synthetic data, showed that the standard error is almost uncorrelated with the actual velocity error (synthetic model - inversion model) and that the mean absolute velocity error is nearly twice the standard error.
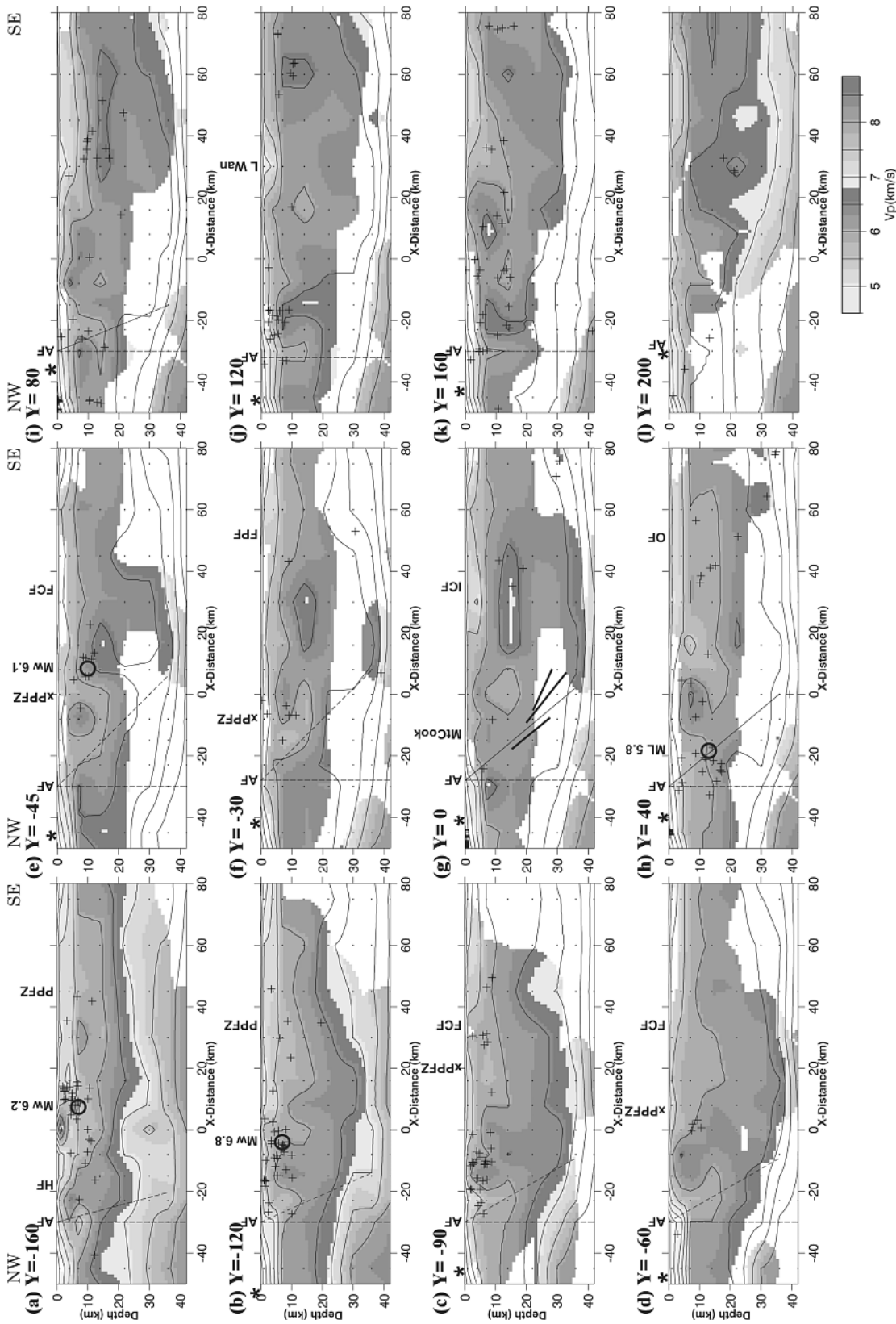
**Figure 8.** Y cross sections of *Vp* model. Areas with low resolution (DRE < 5) are masked but contoured. Each section shows hypocenters (pluses) midway to next section. Small dots indicate velocity nodes. Stars at the top of sections denote the coastline. Dip of Alpine fault is not known, so both vertical and dipping lines are shown. Locations are indicated for the Alpine fault (AF), Hope fault (HF), Porters Pass fault zone (PPFZ) and incipient PPFZ (xPPFZ), Forest Creek fault (FCF), Fox Peak fault (FPF), Mt. Cook, Irishman's Creek fault (ICF), Ostler fault (OF), Lake Wanaka. Reflectors from CDP line [*Okaya and Henrys*,1999] are shown in orange in Figure 8g. Circles show significant earthquakes. See color version of this figure at back of this issue.
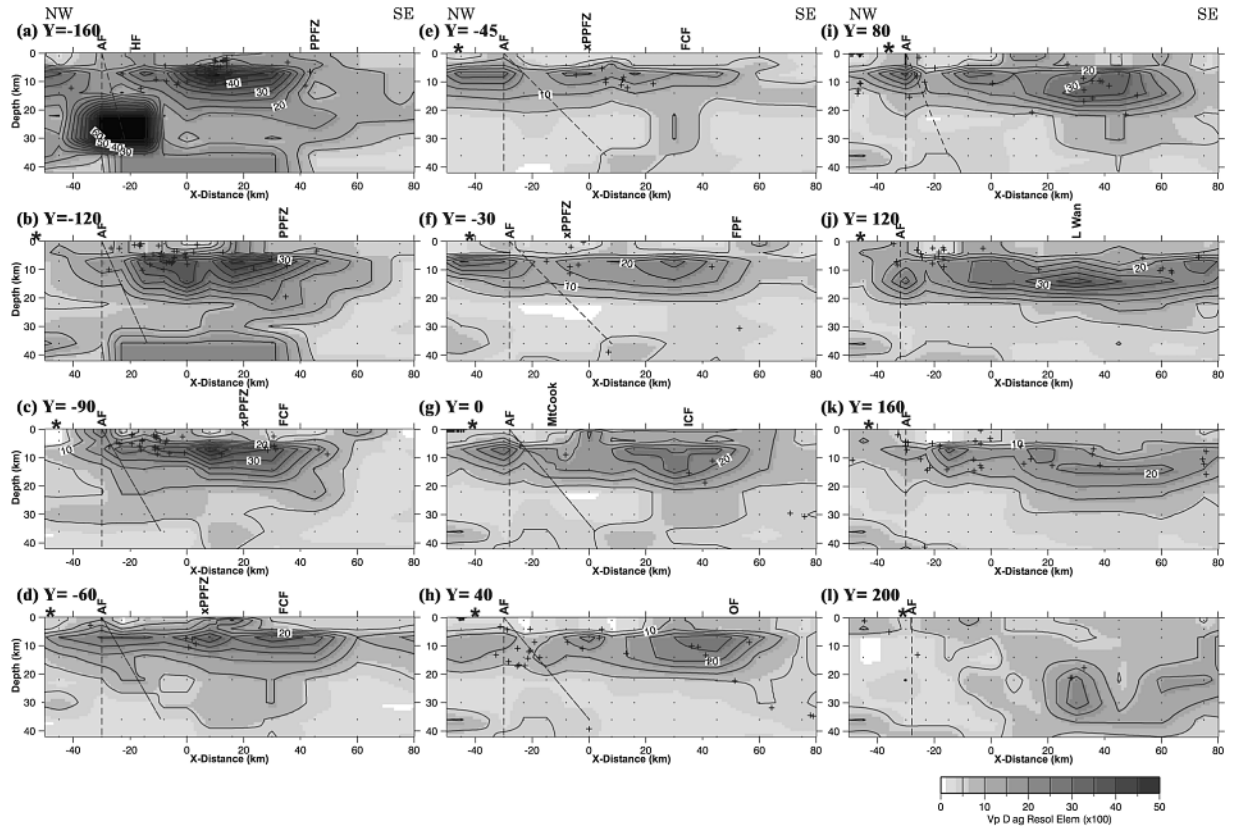
**Figure 9.** Y cross sections of *Vp* resolution. Each section shows hypocenters (pluses) midway to next section. Small dots indicate velocity nodes. Stars at the top of sections denote the coastline. Dip of Alpine fault is not known, so both vertical and dipping lines are shown. Locations are indicated for the Alpine fault (AF), Hope fault (HF), Porters Pass fault zone (PPFZ) and incipient PPFZ (xPPFZ), Forest Creek fault (FCF), Fox Peak fault (FPF), Mt. Cook, Irishman's Creek fault (ICF), Ostler fault (OF), Lake Wanaka.

Thus a conservative estimate of the velocity error is 0.1–0.2 km/s. This is consistent with the comparison in Figure 4, where the velocity patterns are robust, but the actual velocities vary by ±0.2 km/s.

[26] The velocity from 5 to 20 km depth is relatively uniform, ranging from 5.5 to 6.5 km/s (Figure 8). The color scale has been selected to emphasize crustal velocity variations, although the variations are not dramatic. These velocities are typical of graywacke and schist, and the relative uniformity would indicate that there are not large bodies of other exotic rocks present. *Christensen*'s [1999] laboratory measurements of numerous South Island rock samples give 6.1 km/s for Torlesse graywacke and 6.5 km/s for greenschist, at 14-km depth pressure. The *Vp/Vs* tends to be relatively low for the Torlesse graywacke and Haast schist (Figure 1). *Vp/Vs* < 1.65 is imaged within 20-km southeast of the Alpine fault where the Haast schist is narrow (Figures 6a–6d, y = −160 to −90) and throughout the region (Figures 6h–6i, y = 40, 80) where the Haast schist broadens to extend across the South Island. *Vp/Vs* is more moderate for the Caples terrane farther south (Figure 6l, y = 200). Measured *Vp/Vs* is less than 1.70 for Torlesse graywacke samples but tends to be higher and more variable (1.67–1.87) for greenschist samples [*Chris-*

*tensen*, 1999]. In-situ *Vp/Vs* properties sampled by earthquake data (2–20 Hz) may differ from higher frequency (1 MHz) laboratory measurements. Anisotropy may also play a role for *S* picks. A wide range of *P* ray paths will give an average *Vp*, but for each *S* ray path there will be both fast and slow components, and seismic analysts may pick the faster *S*.

[27] Low velocity is associated with faults. A southeast dipping low-velocity zone is associated with the central Alpine fault and a more vertical low-velocity zone is associated with the southern vertical section of the Alpine fault (Figure 8). Given our sparse data, our grid is fairly coarse and so there may be other smaller low-velocity zones that we do not image. Similarly the broad low-velocity zones may represent narrower features with greater velocity reductions. The southeast-dipping Alpine fault low-velocity is most prominent in the y = −60 cross section.

[28] The character changes at y = −30, where the Alpine fault is characterized as a velocity gradient with a large region of low velocity above and southeast of the fault. This above-fault low-velocity feature is spatially limited to a roughly 40-km long region north of Mt. Cook, as it is not imaged on the y = 0 cross section. The resolution is fairly
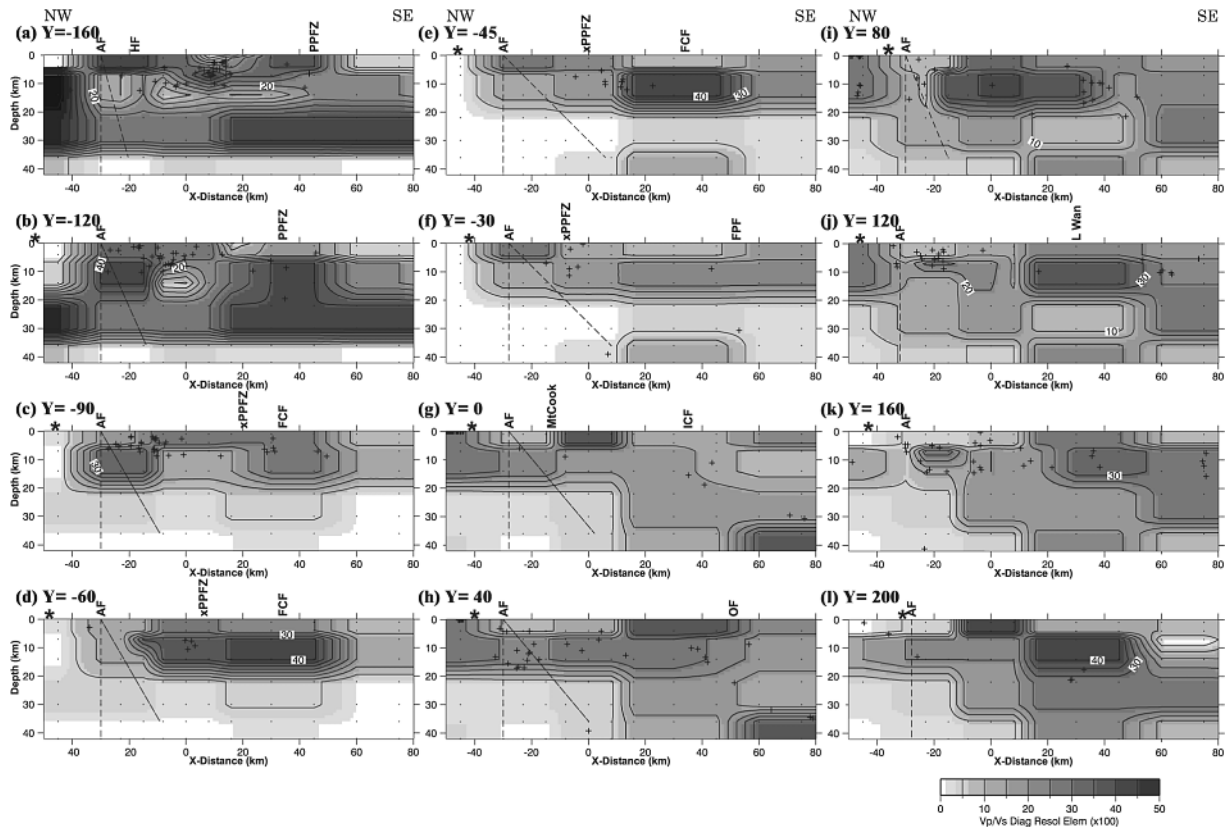
**Figure 10.** Y cross sections of $Vp/Vs$ resolution, with linked nodes. Each section shows hypocenters (pluses) midway to next section. Small dots indicate velocity nodes. Stars at the top of sections denote the coastline. Dip of Alpine fault is not known, so both vertical and dipping lines are shown. Locations are indicated for the Alpine fault (AF), Hope fault (HF), Porters Pass fault zone (PPFZ) and incipient PPFZ (xPPFZ), Forest Creek fault (FCF), Fox Peak fault (FPF), Mt. Cook, Irishman's Creek fault (ICF), Ostler fault (OF), Lake Wanaka.

uniform above 14-km depth and so the extent of the low-velocity feature is realistic.

[29] There are no clear fault-related features in the $Vp/Vs$ solution (Figure 6). However, since the resolution of $Vp/Vs$ is weak, it would be difficult to image small-scale features. If the low $Vp$ regions were related to high fluid pressures, high $Vp/Vs$ may be expected [*Eberhart-Phillips et al.*, 1989]. There is a slight increase in $Vp/Vs$ near the Alpine fault from $y = -60$ to $-30$, but this may be related to different lithology on the northwest side of the fault rather than the fault zone itself. There is higher $Vp/Vs$ below the southern Alpine fault ($y = 80$ to 200) where non-Torlesse rocks adjoin the fault. Measured $Vp/Vs$ is higher (1.77) for southern plutonic rock samples [*Christensen*, 1999].

[30] A prominent high-velocity body is imaged at 14-km depth 50-km southeast of the central Alpine fault and northwest of the Fox Peak fault (Figures 8e–8g, $y = -45$ to 0, Figure 11b, $z = 14$). It is 10–25 km wide and 40–50 km long with velocity greater than 6.5 km/s. The resolution (Figure 9) is adequate at 7–14 km depth and thus the shape of the high-velocity body is realistic. There is a small velocity reversal below the high-velocity body. There is less resolution at that depth, but a velocity reversal is

clearest at $y = 0$ where the 22–30-km-depth resolution is best, and the shape of the high-velocity body is stable regardless of varying strategies for linking nodes. Thus it is likely that the high-velocity body is a distinct feature separate from the 6.5 km/s velocity near the base of the crust.

[31] Comparisons of plan views of the velocity solution and the geology (Figure 1) show that the velocity of the graywacke is generally lower than the schist. At 7–14-km depth (Figures 11a and 11b), the schist south of the Waitaki ($y = 40$) tends to have $Vp > 6.25$ km/s and the material with $Vp > 6.25$ southeast of the Alpine fault widens to the south in accord with the broadening zone of schist. These characteristics are similar to those found for schist and graywacke in the northern South Island [*Eberhart-Phillips and Reyners*, 1997]. The high-velocity body 50-km southeast of the central Alpine fault is most likely to be schist since it has $Vp$ consistent with schist (Figures 11b and 8f, $y = -30$).

[32] For the Australian plate, there are fewer ray paths and the resolution is generally low (Figure 9). The north-ernmost cross section has the best resolution and it shows somewhat higher velocity ($Vp > 6.3$ km/s at 14-km depth)
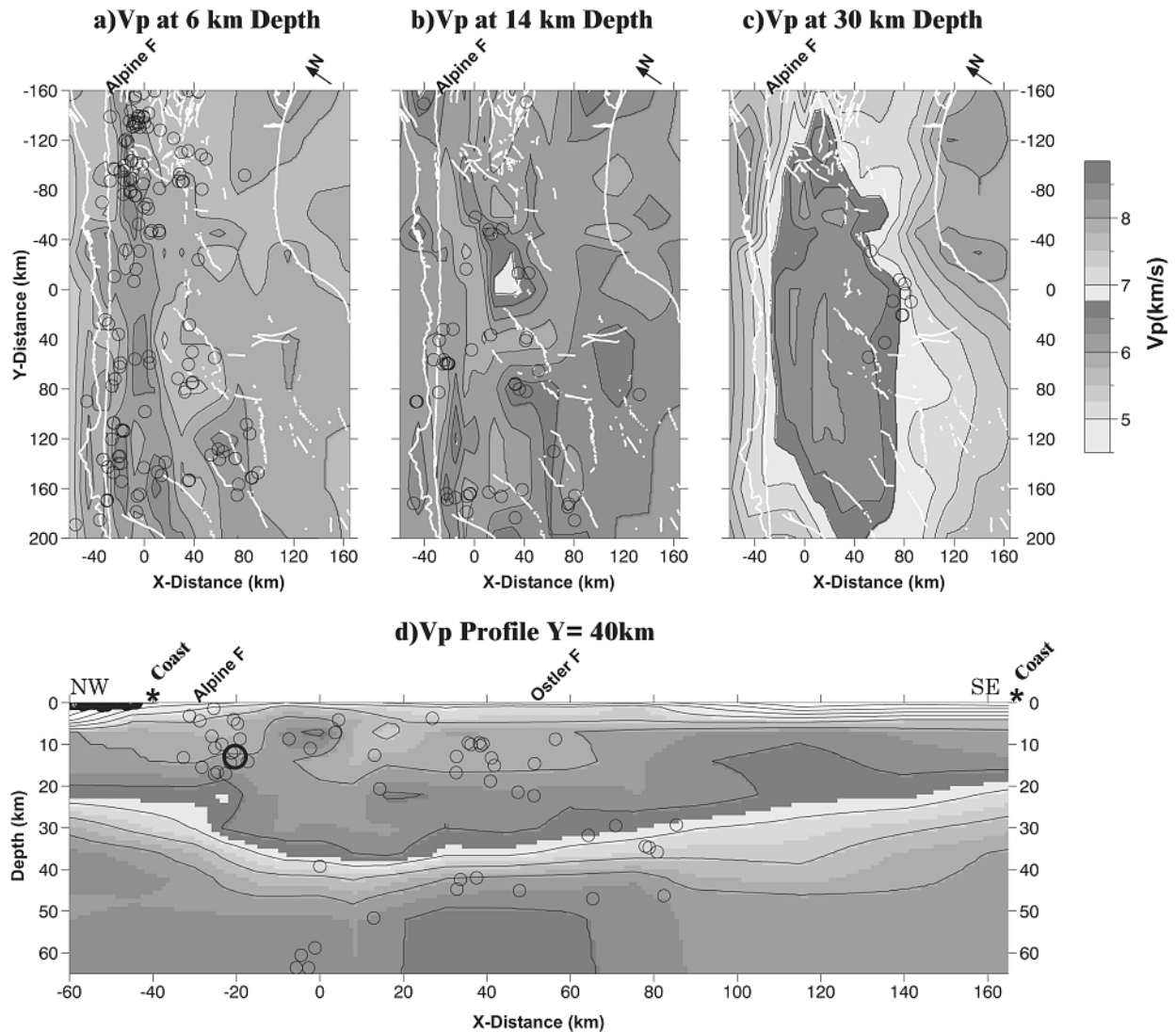
**Figure 11.** Map-views of 3-D $Vp$ model at (a) 6-km depth, hypocenters 2.5 to 10.5 km depth, (b) 14-km depth, hypocenters 10.5 to 22 km depth, (c) 30-km depth, hypocenters 22 to 36 km depth; star indicates Mt. Cook. (d) $y = 40$ cross section to 65-km depth; hypocenters from $y = 0$ to 80 km are shown as circles, including the 1998 $M_L$ 5.8 in bold; simplified faults in white; compare to Figure 2. See color version of this figure at back of this issue.

for the onshore material west of the Alpine fault, as do most of the other cross sections. Also, the $Vp/Vs$ tends to be greater than for the graywacke (>1.70). This is similar to observations of the same terrane of marbles, sandstones and limestones farther north [*Eberhart-Phillips and Reyners*, 1997]. Offshore, farther west, the velocities 30–70 km west of the Alpine fault tend to be lower (Figure 4e), similar to the transect 2 active-source model [*Scherwath et al.*, 2000], which may be partially due to marine sediments.

[33] Along the east coast, the slightly low velocity is consistent with relatively thick sediments. However, on the northeastern peripheral grid, there is higher-velocity imaged at $x = 90–115$ (Figures 11a and 11b). This is caused by smearing of high-velocity from volcanics of the Banks Peninsula where the nearest seismic station is located. In a previous study [*Leitner et al.*, 2001] this station had a time

delay correction indicative of fast velocity and less sediment.

[34] The deep structure, shown as isovelocity surfaces in Figure 12, is primarily influenced by the gravity inversion. Thus the resolution is fairly even spatially, but small features may not be imaged. A lower-crustal velocity of about 7.0 km/s has been inferred to represent gabbroic Mesozoic oceanic crust that has underlain the Torlesse terrane since its accretion [*Smith et al.*, 1995; *Godfrey et al.*, 2001]. The 7.0 km/s surface can be used to approximate the crustal root, which is formed from relatively low-velocity crustal material which has moved downward during compression (Figure 2). It shows that the crustal root under the Southern Alps contains material less than 7.0 km/s to 35–39 km depth, with the deepest part at $y = 80$, 45-km southeast of the Alpine fault. The crustal root has a sharp gradient on the northwest side near the Alpine fault, south
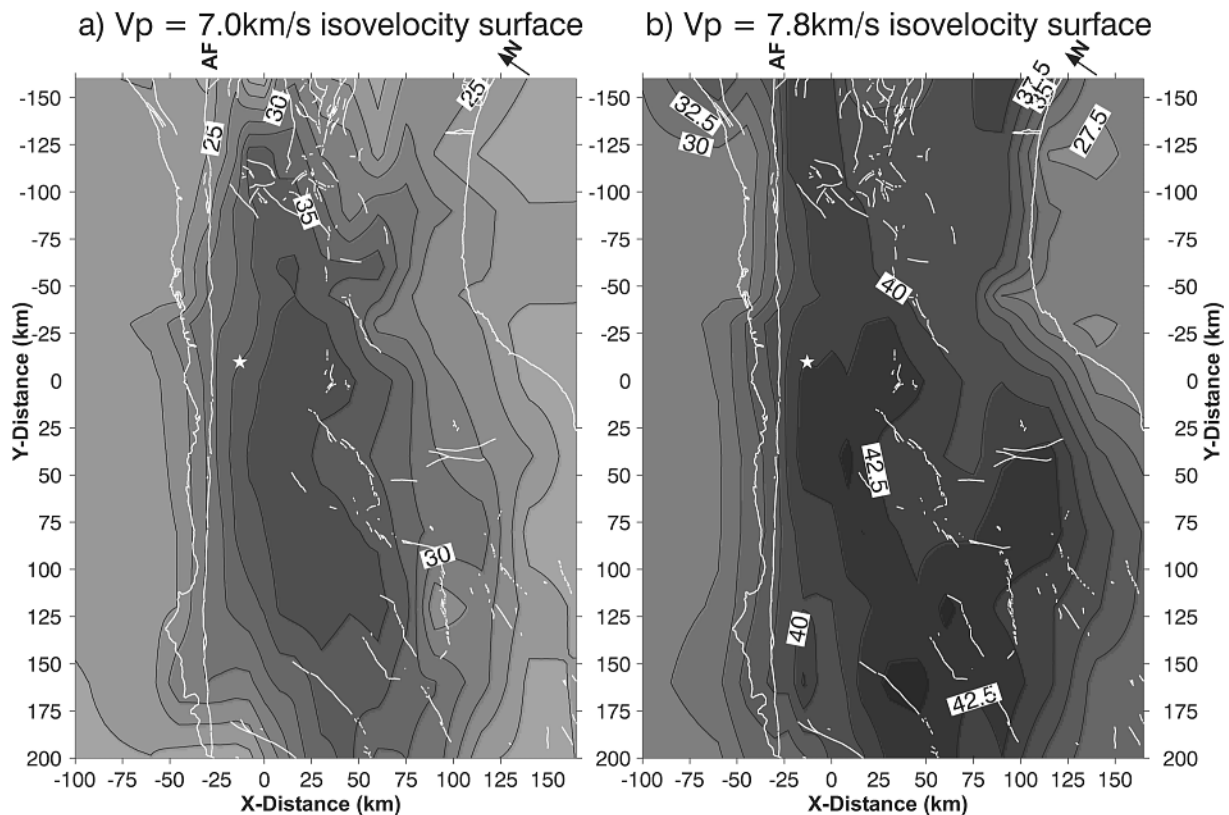
**Figure 12.** Plots of (a) 7.0 and (b) 7.8 km/s isovelocity surfaces. Contour interval is 2.5 km depth; star indicates Mt. Cook.

of Mt. Cook. North of Mt. Cook, the orientation of the northwest-side gradient is rotated away from the Alpine fault. Our inversion does not solve for any discontinuities, but rather for velocities on a grid with linear gradients between the grid nodes. Therefore we cannot give a definite estimate of the Moho discontinuity. However, the 7.8 km/s isovelocity surface can be used to approximate the 3-D shape of the Moho since crustal velocities are less than 7.8 km/s, including the lower crust. This shows regional variations in addition to the Southern Alps crustal root. The Moho is almost 10 km deeper in Otago than Canterbury. The deepest part of the Moho extends into Fiordland, in contrast to the crustal root that is limited to the Southern Alps.

## 5. Discussion

### 5.1. Alpine Fault

[35] Low-velocity zones are often observed in association with faults [*Eberhart-Phillips et al.*, 1995]. Substantial low-velocity zones have been imaged along the creeping section of the San Andreas fault [*Mooney and Ginzburg*, 1986; *Thurber et al.*, 1997], and along the New Madrid fault zone [*Al-Shukri and Mitchell*, 1988]. Narrow low-velocity zones (<300 m) have been identified at active fault sites such as Parkfield and Landers where high-quality data are available [*Leary and Ben-Zion*, 1992; *Li et al.*, 2000]. In the Marlborough fault system northeast of the Southern Alps region,

a strong vertical low-velocity zone is imaged along the Awatere fault [*Eberhart-Phillips and Reyners*, 1997], which is a major active fault that experienced a magnitude 7.5 earthquake in 1848.

[36] Along the Alpine fault, southwest of Haast where the fault is primarily strike-slip with less than 3 mm/yr dip slip [*Norris and Cooper*, 2000], our results show a vertical low-velocity zone to at least 15 km depth (Figures 8i–8l, $y = 80$ to 200). North of Haast where the dip slip ranges from 6 to over 12 mm/yr [*Norris and Cooper*, 2000], there is a broad dipping low-velocity zone to at least 15 km depth (Figures 8b–8h, $y = -120$ to 40). The velocity is reduced by about 0.25 km/s or 4%. Greater velocity reduction over thinner zones is also consistent with our data. The low-damping solution (Figure 4b) gives 7–16% velocity reduction along the Alpine fault; however, the data fit is only slightly better. Given our sparse data, we cannot discern whether there is an additional narrow very low-velocity zone within the broad feature.

[37] Seismic reflection data has revealed reflectors possibly associated with the deep fault zone. Reflections between 9–15 s two-way travel time, with reverse move out, were recorded on a seismic line east of the Alpine Fault, beside Lake Pukaki [*Davey et al.*, 1995]. These reflections help define a boundary about 22–25 km deep and dipping about 40° to the southeast, that, when projected to the surface, roughly coincides with the surface trace of the Alpine Fault [*Davey et al.*, 1995]. Low-fold stacked images

reveal a bright reflective zone up to 4 s thick, the top of which extends from about 24-km depth and bends downward beneath the Southern Alps to about 30-km depth [*Davey et al.*, 1998]. The most accurate locations of reflectors observed in the Mt. Cook CDP line have been determined by prestack migration [*Okaya and Henrys*, 1999] and are shown in Figure 8g, $y = 0$. The reflections are in the ductilely deforming region and may indicate a broad deformation zone for the deep fault, in contrast to the planar structure associated with rupture in the shallower brittle fault zone. *Stern et al.* [2001] on T2 also infer a low-velocity zone in the vicinity of the deep fault, with a speed reduction of 6–10%, on the basis of travel time delays from wide-angle reflections and teleseismic *P* waves.

[38] There is some indication of low velocity along other faults, but not to the same degree as observed along the Alpine fault. Low velocity may be associated with regions of active faults near the recent reverse Cass (moment magnitude ($M_w$) 6.2) and Arthur's Pass ($M_w$ 6.8) earthquakes (Figures 8a and 8b, $y = -160, -120$). There is low velocity in the vicinity of the incipient Porters Pass fault zone, particularly near the strike-slip Godley River ($M_w$ 6.1) earthquake (Figure 8e, $y = -45$).

[39] Faults may have low velocity because of gouge, high crack density and high pore pressure [*Eberhart-Phillips et al.*, 1995]. Measurements of gouge show that it can have a velocity 20% lower than the country rock [*Wang et al.*, 1978]. Gouge results from brittle deformation, and may especially be a factor in the low velocity along the southwestern vertical fault zone. Theoretical formulas show that for increasing crack density, velocities decrease and $Vp/Vs$ increases [*O'Connell and Budiansky*, 1974]. An increase in low-aspect ratio (flat) microcracks will have a large velocity reduction effect, even though it may represent an almost negligible increase in porosity [*Toksoz et al.*, 1976]. Both laboratory measurements [*Todd and Simmons*, 1972] and theoretical formulas [*Toksoz et al.*, 1976] show that near-lithostatic fluid pressure can cause large velocity reduction and also will serve to exaggerate and preserve the effect of high crack density. Increasing pore pressure requires some fluid input from metamorphic processes; however, large fluid volumes are not required for low-porosity rocks. Thus, increased crack density and high fluid pressure in the vicinity of Alpine fault deformation could cause the observed velocity reduction.

[40] Temperature and active strain are other factors that can produce velocity reduction and may be contributing factors, particularly in the fully ductile zone. Thermal modeling of the Alpine fault shows a broad zone of elevated isotherms toward the Alpine fault [*Shi et al.*, 1996]. Laboratory measurements of metagraywacke show that such a temperature increase can cause a 1–2% velocity reduction at 15–30 km depths [*Christensen and Mooney*, 1995]. Active straining of rock also produces small decreases in velocity, as observed in laboratory studies of dynamic moduli [*Winkler and Murphy*, 1995].

[41] The strongest effect of strain is anisotropy related to the total permanent strain that the rock has experienced. South Island schists are highly anisotropic with anisotropy up to 17% [*Okaya et al.*, 1995]. However, in our 3-D study we have a wide azimuthal range of ray paths (Figure 3) and anisotropy is unlikely to be a primary factor in the observed velocity heterogeneity. A feature like the Alpine fault low-velocity zone that continues throughout the 3-D model regardless of variations in the ray path azimuthal distribution, cannot be readily attributed to anisotropy. Recent inversions for 3-D velocity with anisotropy in the Marlborough region find the isotropic component of velocity is very similar to that found from an isotropic inversion, although up to 15% crustal anisotropy is found and the model that includes anisotropy fits the data better [*Eberhart-Phillips and Henderson*, 2001].

## 5.2. Convergence Structure

[42] The $y = 40$ cross section (Figure 11d) is easiest to relate to the models of obliquely convergent plate boundary (Figure 2), since it is fully south of the influence of the Marlborough fault zone and the Porters Pass fault zone [*Leitner et al.*, 2001]. This is the region where some deep Southern Alps earthquakes have been observed, and where there was a widely felt local-magnitude ($M_L$) 5.8 earthquake near the Alpine fault in 1998. Refraction 2-D models show a 5–10 km thick lower crustal layer of oceanic crust underlying the graywacke crust [*Davey et al.*, 1998]. The earthquakes deeper than 25 km occur in the oceanic crust and uppermost mantle. The graywacke crust is interpreted to move through the root, with a portion moving up along the Alpine fault and backthrusts, and a portion remaining in the root (Figure 2). There is significant seismicity near the Alpine fault which appears to dip more steeply than 45°. The other shallow seismicity may be related to backthrusts, which are also associated with relatively low velocity.

[43] During oblique convergence, the mantle moves downward (Figure 2). Using teleseismic delays, *Stern et al.* [2000] and *Kohler and Eberhart-Phillips* [2002] image mantle deformation as a high-velocity body to 150-km depth centered below the crustal root. They show that it is incompatible with a subducting Pacific plate slab model and rather suggest that the mantle deforms continuously. The local earthquake data also show high-velocity mantle below the crustal root (Figure 11d). If the mantle is deforming continuously, then the behavior of the lower crust must be addressed. It is most likely being underplated below the crustal root, as has been suggested by *Van Avendonk et al.* [1999]. Where the lower crust has been imaged in offshore seismic reflection data, it appears to be of variable thickness, as though it has experienced deformation [*Mortimer et al.*, 2002]. Thus it is unlikely to be a uniform strong layer and it may be amenable to fracture and underplating. The region extending from the base of the lower crust to the deepest earthquakes may be the region that is accommodating the underplated lower crust (Figure 11d). Note that there are only a few deep earthquakes and only in the region near the deepest crustal root. As described by *Shi et al.* [1996] the isotherms in the lower crust and mantle are depressed by lithospheric thickening, and they will be most depressed where the crustal root is greatest.

## 5.3. Rigid High-Velocity Body and Adjoining Low-Velocity Body

[44] Where the plate boundary deformation zone is much narrower in the central section, the velocity model is much different. Considering the 14-km depth slice near $y = -30$ (Figure 11b), the image is dominated by the high-velocity

schist body which is paired with the large low-velocity feature northeast of Mt. Cook. Thus there may be a causal relationship between the adjoining features. The high-velocity schist body would be drier and more rigid than the surrounding graywacke in the incoming crust. It may act to concentrate ductile shear deformation in the adjoining low-velocity region and so be partially responsible for the narrower plate boundary deformation zone. The more rigid body would also reduce deformation at its location, as seen in the landforms. Its location is roughly related to the MacKenzie Basin, which stands out as a relatively flat area within the rugged Southern Alps.

[45] The edges of the high-velocity body may be related to Cretaceous and Cenozoic faults (Figures 11b and 8e–8g). The southern edge may be related to the Irishman's Creek fault, which dips to the southeast. The eastern edge is subparallel to the Forest Creek and Fox Peak faults, which dip to the west. Torlesse graywacke was accreted and experienced convergent tectonics and regional metamorphism from the Jurassic until early Cretaceous, creating the Haast schist (Figure 1), with metamorphism peaking at 170–180 Ma [*Little et al.*, 1999; *Mortimer*, 1993, 1995]. Rocks of different metamorphic grade were subsequently juxtaposed by postmetamorphic Cretaceous normal faults, including the Irishman Creek fault and faults within the Waitaki-Waihemo fault zone, so that blocks of schist and semischist adjoin graywacke [*Forsyth*, 2002; *Mortimer*, 1993; *Gair*, 1967; *Long and Cox*, 2002]. The high-velocity schist body is likely to have been emplaced during the Cretaceous normal faulting. A long stable period of erosion and cover followed, which would have led to relatively uniform crustal thickness. Mid-Miocene tectonics bent the South Island terranes and Haast schist belt (Figure 1) and brought about reverse faulting on north-northeast trending faults such as the Fox Peak and Ostler faults [*Wood and Begg*, 1990], while reactivating previously normal faults, such as the Irishman Creek fault, with reverse slip [*Bishop*, 1974; *Long and Cox*, 2002]. Ductile processes have thickened the lower crust, including under the high-velocity schist. The slightly lower velocity of the thickening lower crust appears as a velocity reversal under the high-velocity upper crustal feature.

[46] The high-velocity body corresponds to the high-resistivity feature in the Southern Alps model of magnetotelluric observations [*Wannamaker et al.*, 2002]. If the feature represents Mesozoic schist, it would be depleted of fluids and have high-resistivity. In Figure 13, the feature with resistivity >3000 ohm m has the same spatial dimension as the high-velocity feature and extends to 20-km depth. The high-resistivity feature extends to the surface, but that may be due to separate localized near-surface blocks. The adjoining low-velocity area to the northwest, where concentrated deformation is inferred, is associated with low resistivity (<300 ohm m). *Wannamaker et al.* [2002] suggest that the low resistivity is due to metamorphic fluids, which result in particularly high conductivity in actively deforming ductile regions, as fluid is distributed throughout grain boundaries [*Tullis et al.*, 1996]. This increased fluid surface area within the ductilely deforming rock volume will also act to decrease seismic velocity, since its effect will be similar to increasing fracture density without changing porosity [*O'Connell and Budiansky*,

1974; *Toksoz et al.*, 1976]. The low-resistivity zone does not extend to the upper 7 km of the Alpine fault because those rocks have been mechanically depleted of fluids as they crossed the brittle-ductile transition [*Wannamaker et al.*, 2002]. The U-shaped low resistivity does extend under the high-resistivity body and up to the surface on the southeast. The velocity reversal at 22-km depth below the high-velocity body is thus correlated with the southeastern side of the zone of low-resistivity metamorphic fluids. This zone reaches the surface near the Forest Creek fault zone, which *Upton et al.* [2000] suggest is a major backthrust to the Alpine fault on the basis of recent movement and fluid isotopes. The seismic image is consistent with reverse faulting on this structure, but the image is too coarse to confirm a distinct low-velocity fault zone.

[47] Below the low-velocity low-resistivity region, there is an area of increased velocity that may be an inversion artifact that is indirectly related to overlying high fluid pressure. This increased velocity below 20 km is only seen on the $y = -45$ and $-30$ cross sections (Figures 8e–8f). This feature resulted from the gravity inversion, and is not required for the travel time data, which have little resolution at that depth. It may indicate a problem, in this specific part of the 3-D model, with the general velocity–density relationship used to compute gravity from 3-D velocity. If the low-velocity is caused by high fluid pressure and high fracture density, instead of varied lithology or porosity, then the density estimated from the velocity will be too low and the gravity inversion would favor increased density (velocity). Thus, this possible artifact is further evidence that the low-velocity region is caused by high fluid pressure and increased fluid surface area of ductile deformation.

[48] Excess fluids with high fluid pressure would increase $Vp/Vs$. The large low-velocity region in $y = -30$ stands out in the $Vp/Vs$ solution by having increased $Vp/Vs$ below 4-km depth, but it does not exhibit unusually high values. Thus it is consistent with high fluid pressure, although it does not confirm it. A relatively narrow 20-km deep zone of high conductivity [*Wannamaker et al.*, 2002] or shallow fluids confined to narrow fracture zones [*Upton et al.*, 2000] would not be imaged with our sparse $S$ data.

## 5.4. Comparison to 2-D Profile

[49] Different data and analysis techniques will give different images of the same region. Comparing different results helps to show key common features and to convey uncertainties; for example, we consider transect 1. *Van Avendonk et al.* [1999] use reflection and refraction travel times from surface sources to solve for both velocity and reflecting boundaries along T1 (Figure 3). Figure 14 compares our 3-D model to the boundaries in their active-source 2-D model. In contrast we use only first arrival times to solve for velocity on a grid and do not include discontinuities, but we additionally include sources (earthquakes) throughout the modeled volume. Thus the 3-D model will tend to have a smooth gradient where it has low resolution and the 2-D model will tend to have uniform velocity separated by sharp discontinuities where it has low resolution. The derived velocities in the 2-D and 3-D models are very similar, which shows the reliability of the data and the utility of both inversion techniques.
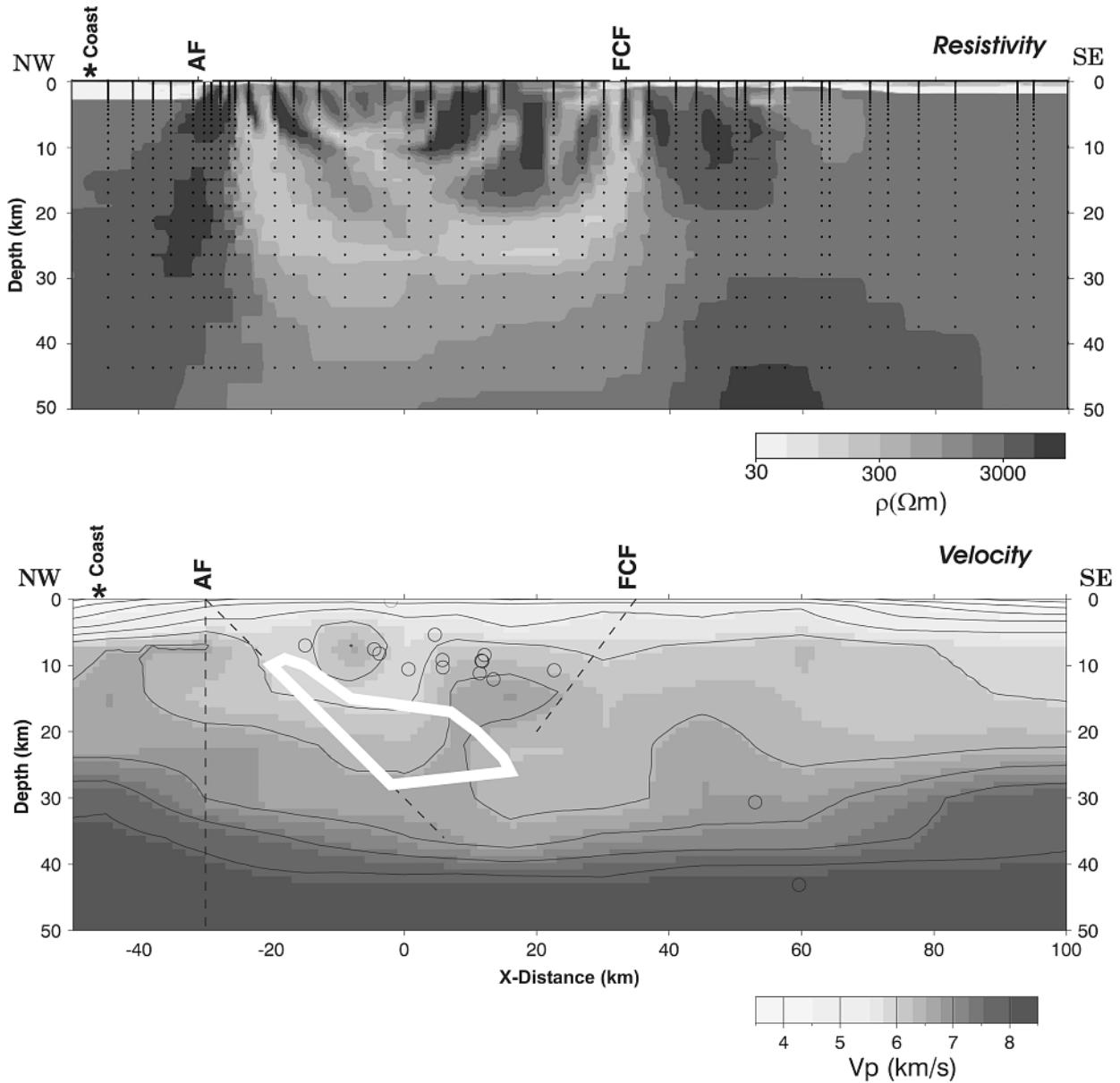
**Figure 13.** (a) Resistivity model for magnetotelluric data [*Wannamaker et al.*, 2002]. (b) *Vp* model at same location, $y = -45$ km. High velocity is related to high resistivity, and adjacent low velocity may represent a region of concentrated deformation, as sketched with the white line. Faults are schematic as true dips at depth are unknown.

[50] The reflection tomography includes a shallow basin interface, which is a discontinuity of 4.5 to 5.5 km/s. In the 3-D model this is a gradient over $2-4$ km. The pattern of velocity in the upper 15 km is similar in both models. The minor high-velocity feature between 20 and 40 km southeast of the Alpine fault and the generally lower-velocity feature about 60 km southeast of the Alpine fault are also imaged in the 2-D model [*Van Avendonk et al.*, 1999]. The high-velocity feature is slightly deeper in our model. This is likely to be realistic since we have earthquake sources in the vicinity whereas the active-source model only had surface sources and relied on reflected arrivals, which sample the average crustal velocities over the ray path to the lower crust or Moho. An intriguing difference in the images is the more prominent low velocity along the Alpine fault in the 3-D model below 10 km depth, which is only a broad feature in the active-source model [*Van Avendonk et al.*, 1999].

[51] Below 15 km the velocities are also similar. The 6.5 and 7.0 contours in the 3-D model are close to the 2-D model bounds of the lower crust which has velocities about $6.5-7.0$ km/s. The 2-D model Moho has a sharp discontinuity of about 7.0 to 8.0 km/s, while the approximated Moho in the 3-D model is a gradient over $3-10$ km. Both show some heterogeneity in mantle velocity, with a region
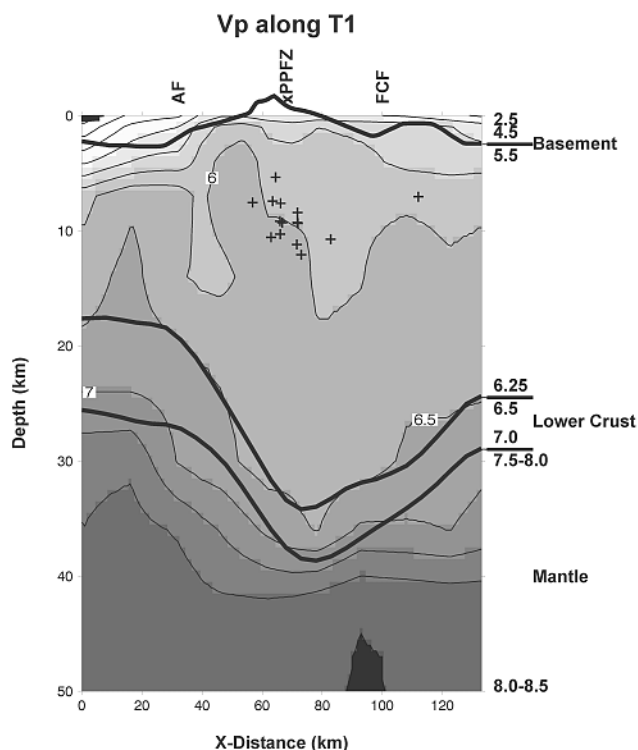
**Figure 14.** Comparison of 3-D velocity (contoured gray scale image) and T1 (Figure 3) model of *Van Avendonk et al.* [1999], hypocenters within 15 km are shown. T1 model is shown by layer boundaries in heavy lines, and the velocity range of layers (km/s) is labeled on the right.

of reduced uppermost mantle velocity located west of the crustal root and relatively high velocity underlying the crustal root.

### 5.5. Crustal Root and Moho

[52] The approximate Moho, shown by the 7.8 km/s surface (Figure 12b), is consistent with the active source profiles. It is also consistent with receiver function data [*Parker*, 1999]. The receiver functions for the two stations on the eastern side of the Southern Alps have similar Moho *P*-to-*S* conversions and a Moho similar to that estimated in our model, while the station in eastern Otago has a 1-s earlier *P*-to-*S* conversion, as expected for a roughly 10 km shallower Moho in eastern Otago.

[53] The 3-D velocity results show regional variation in the Moho of the incoming Pacific plate, with a crustal thickness in Otago 5–10 km greater than Canterbury (Figure 12b). The change occurs at $y = 40$ in the vicinity of the WWFZ, in accord with a change in tectonics to a broader southern deformation zone. *Koons et al.* [1999] show that the incoming thicker crust is weaker and thus is a key factor in the widening of the orogen south of the WWFZ.

[54] The crustal root is asymmetric with a sharper gradient on the western side. The relatively sharp boundary throughout the crust supports the case put by *Sutherland et al.* [2000] that there is a major lithospheric discontinuity since the Eocene which determines the location of the current Alpine fault. This also supports the idea that the Australian plate can be modeled as a rigid indentor [*Norris*

*et al.*, 1990; *Shi et al.*, 1996]. Numerical modeling by *Koons et al.* [1998] shows that there may be a near-vertical zone of dextral shear below 15-km depth on the northwest margin of the deforming region.

[55] The shape of the crustal root, with the deepest crust roughly 80-km south of Mt. Cook (Figure 12a), is not directly correlated with the amount of convergence, as *Walcott* [1998] shows that the northern part has experienced about 25% more convergence over the last 12 Myr. In 2-D numerical models, *Shi et al.* [1996] allow proportionally more crustal material to go into the root in southern profiles. However, in 3-D models of convergence, *Gerbault and Davey* [2002] show that the large southern thickening is a result of lateral extrusion of ductile lower crust because a broader zone of thickening requires less energy than localized vertical thickening. The 3-D model of *Gerbault and Davey* [2002] results in a crustal root similar to that imaged by our velocity inversion, approximately 300-km long, oriented about 10° from the Alpine fault, and having greatest thickness near $y = 80$. North of Mt. Cook, the imaged crustal root is smaller and oriented more nearly parallel to the Alpine fault.

## 6. Conclusions

[56] The inversion of combined earthquake and active source data images the 3-D *Vp* and *Vp/Vs* crustal structure of the Southern Alps region. Linked nodes are valuable in sparsely sampled areas to obtain a useful model. Inversion of gravity data further refined the velocity model below 20-km depth where travel time data provide little resolution.

[57] The velocities are generally related to lithology and terranes. Crustal *Vp* is relatively uniform from 5.5 to 6.5 km/s, typical of graywacke and schist. Areas of mapped schist tend to have slightly higher velocity, with *Vp* > 6.2 at 7-km depth.

[58] Low-velocity zones are imaged along the Alpine fault, southeast dipping in the central region and vertical in the southern vertical strike-slip section. A combination of increased crack density, high pore pressure, increased temperature, and active strain may cause this velocity reduction.

[59] The 3-D model is consistent with models of oblique convergence, with the upper crust forming both uplifted mountains and a crustal root, the underlying oceanic lower crust being fractured and underplated and the upper mantle translating downward through continuous deformation.

[60] A high-velocity, high-resistivity body is imaged in the eastern Southern Alps, and is inferred to represent relatively rigid Mesozoic schist. The body may act to constrain the orogen by reducing deformation in the overlying MacKenzie basin and concentrating ductile shear deformation in the adjoining low-velocity region northeast of Mt. Cook.

[61] The imaged crustal root is asymmetric with a sharper gradient on the western side, consistent with a relatively rigid Australian plate, and it has its deepest part 80 km south of Mt. Cook, consistent with numerical modeling that includes a ductile lower crust.

[62] This work provides information that can be used to investigate how material properties affect rupture propagation and 3-D heterogeneity in rheology influences strain. It

can also provide the crustal model for teleseismic tomography. The data are sparse in many areas. In the future, denser deployments in key areas would improve definition of specific structures and tectonic features.

# References

Al-Shukri, M. J., and B. J. Mitchell, Reduced seismic velocities in the source zone of the New Madrid earthquake, *Bull. Seismol. Soc. Am.*, *78*, 1491–1509, 1988.

Anderson, H., D. Eberhart-Phillips, T. McEvilly, F. Wu, and R. Uhrhammer, Southern Alps passive seismic experiment, *Sci. Rep. 97/21*, Inst. of Geol. and Nucl. Sci., Lower Hutt, New Zealand, 1997.

Beavan, J., and J. Haines, Contemporary horizontal velocity and strain rate fields of the Pacific-Australian plate boundary zone through New Zealand, *J. Geophys. Res.*, *106*, 741–770, 2001.

Beavan, J., M. Moore, C. Pearson, M. Henderson, B. Parsons, S. Bourne, P. England, D. Walcott, G. Blick, D. Darby, and K. Hodgkinson, Crustal deformation during 1994–1998 due to oblique continental collision in the central Southern Alps, New Zealand, and implications for seismic potential of the Alpine fault, *J. Geophys. Res.*, *104*, 25,233–25,255, 1999.

Bijwaard, H., W. Spakman, and E. R. Engdahl, Closing the gap between regional and global travel time tomography, *J. Geophys. Res.*, *103*, 30,055–30,078, 1998.

Bishop, D. G., Stratigraphic, structural and metamorphic relationships in the Dansey Pass area, Otago, New Zealand, *N. Z. J. Geol. Geophys.*, *17*, 301–355, 1974.

Christensen, N. I., Physical and chemical properties of South Island, New Zealand rocks, report, 60 pp., Univ. of Wis., Madison, 1999.

Christensen, N. I., and W. D. Mooney, Seismic velocity structure and composition of the continental crust: A global view, *J. Geophys. Res.*, *100*, 9761–9788, 1995.

Davey, F., T. Henyey, S. Kleffmann, A. Melhuish, D. Okaya, T. Stern, and D. Woodward, A possible crustal seismic reflection from the Alpine fault, *N. Z. J. Geol. Geophys.*, *38*, 601–604, 1995.

Davey, F., et al., Preliminary results from a geophysical study across a modern continent–continent collisional plate boundary: The Southern Alps, New Zealand, *Tectonophysics*, *288*, 221–235, 1998.

Eberhart-Phillips, D., Three-dimensional velocity structure in Northern California Coast Ranges from inversion of local earthquake arrival times, *Bull. Seismol. Soc. Am.*, *76*, 1025–1052, 1986.

Eberhart-Phillips, D., Three-dimensional *P* and *S* velocity structure in the Coalinga region, California, *J. Geophys. Res.*, *95*, 15,343–15,363, 1990.

Eberhart-Phillips, D., Local earthquake tomography: Earthquake source regions, in *Seismic Tomography: Theory and Practice*, edited by H. M. Iyer and K. Hirahara, pp. 613–643, Chapman and Hall, New York, 1993.

Eberhart-Phillips, D., and M. Henderson, Including anisotropy in 3-D velocity inversion and application to Marlborough, New Zealand, paper presented at New Zealand Geophysical Society Symposium 2001, N. Z. Geophys. Soc., Taupo, 2001.

Eberhart-Phillips, D., and A. J. Michael, Seismotectonics of the Loma Prieta, California, region determined from three-dimensional *Vp*, *Vp/Vs*, and seismicity, *J. Geophys. Res.*, *103*, 21,099–21,120, 1998.

Eberhart-Phillips, D., and M. Reyners, Continental subduction and three-dimensional crustal structure: The northern South Island, New Zealand, *J. Geophys. Res.*, *102*, 11,843–11,861, 1997.

Eberhart-Phillips, D., D.-H. Han, and M. D. Zoback, Empirical relationships among seismic velocity, effective pressure, porosity, and clay content in sandstone, *Geophysics*, *54*, 82–89, 1989.

Eberhart-Phillips, D., W. D. Stanley, B. D. Rodriguez, and W. J. Lutter, Surface seismic and electrical methods to detect fluids related to faulting, *J. Geophys. Res.*, *100*, 12,919–12,936, 1995.

Forsyth, P. J., Geology of the Waitaki area, *Geol. Map 19*, scale 1:250,000, Inst. of Geol. and Nucl. Sci., Lower Hutt, 2002.

Gair, H. S., Mt. Cook, sheet 20, scale 1:250,000, Dep. for Sci. and Ind. Res., Wellington, 1967.

Gardner, G. H. F., L. W. Gardner, and A. R. Gregory, Formation velocity and density: The diagnostic basics for stratigraphic traps, *Geophysics*, *39*, 770–780, 1974.

Gerbault, M., and F. Davey, 3-D lateral crustal thickening in continental oblique collision: An example from the Southern Alps, New Zealand, *Geophys. J. Int.*, in press, 2002.

Godfrey, N. J., F. Davey, and T. A. Stern, Crustal structure and thermal anomalies of the Dunedin region, South Island, New Zealand, *J. Geophys. Res.*, *106*, 30,835–30,848, 2001.

Hill, D. P., Seismic evidence for the structure and Cenozoic tectonics of the Pacific Coast States, in *Cenozoic Tectonics and Regional Geophysics of the Western Cordillera*, edited by R. B. Smith and G. P. Eaton, *Mem. Geol. Soc. Am.*, *152*, 145–174, 1978.

Kleffmann, S., Crustal structure studies of a transpressional plate boundary: The central South Island of New Zealand, Ph.D. thesis, 230 pp., Victoria Univ. of Wellington, Wellington, New Zealand, 1999.

Kleffmann, S., F. Davey, A. Melhuish, D. Okaya, and T. Stern, Crustal structure in the Central South Island from the Lake Pukaki seismic experiment, *N. Z. J. Geol. Geophys.*, *41*, 39–49, 1998.

Kohler, M. D., and D. Eberhart-Phillips, Three-dimensional lithospheric structure below the New Zealand Southern Alps, *J. Geophys. Res.*, *107*, 10.1029/2001JB000182, in press, 2002.

Koons, P. O., R. J. Norris, A. F. Cooper, and D. Craw, Mechanics of a single structure accommodating oblique convergence: The development of the Alpine fault, in *Geological Society of New Zealand—New Zealand Geophysical Society Annual Conference, Misc. Publ. 101A*, p. 138, Geol. Soc. N. Z., Lower Hutt, 1998.

Koons, P. O., P. Upton, C. M. Henderson, R. L. Enlow, and C. J. Pearson, Otago versus Canterbury: Basic differences in inherited geology and applied forces, in *Geological Society of New Zealand Annual Conference, Misc. Publ. 107A*, p. 82, Geol. Soc. N. Z., Lower Hutt, 1999.

Leary, P., and Y. Ben-Zion, A 200-m wide fault zone low velocity layer on the San Andreas fault at Parkfield: Results from analytic waveform fits to trapped wave groups, *Seismol. Res. Lett.*, *63*, 62, 1992.

Leitner, B., D. Eberhart-Phillips, H. Anderson, and J. N. Nabelek, A focused look at the Alpine fault, New Zealand: Seismicity, focal mechanisms and stress inversions, *J. Geophys. Res.*, *106*, 2193–2220, 2001.

Li, Y.-G., J. E. Vidale, K. Aki, and F. Xu, Depth-dependent structure of the Landers fault zone from trapped waves generated by aftershocks, *J. Geophys. Res.*, *105*, 6237–6254, 2000.

Little, T. A., N. Mortimer, and M. McWilliams, An episodic Cretaceous cooling model for the Otago-Marlborough Schist, based on $^{40}Ar/^{39}Ar$ white mica ages, *N. Z. J. Geol. Geophys.*, *42*, 305–326, 1999.

Long, D., and S. Cox, Upper crustal structure beneath the Southern Alps-Mackenzie Basin, New Zealand, derived from seismic reflection data, *N. Z. J. Geol. Geophys.*, in press, 2002.

Mooney, W. D., and A. Ginzburg, Seismic measurements of the internal properties of fault zones, *Pure Appl. Geophys.*, *124*, 141–157, 1986.

Mortimer, N., Geology of the Otago Schist and adjacent rocks, *Geol. Map 7*, scale 1:500,000, Inst. of Geol. and Nucl. Sci., Lower Hutt, New Zealand, 1993.

Mortimer, N., Triassic to Early Cretaceous tectonic evolution of New Zealand terranes: A summary of recent data and an integrated model, in *Proceedings of the 1995 PACRIM Congress*, edited by J. L. Mauk and J. D. St-George, pp. 401–406, Austral. Inst. of Min. and Metall., Carlton, Victoria, Australia, 1995.

Mortimer, N., A. J. Tulloch, R. N. Spark, N. W. Walker, E. Ladley, A. Allibone, and D. L. Kimbrough, Overview of the Median Batholith, New Zealand: A new interpretation of the geology of the Median Tectonic Zone and adjacent rocks, *J. Afr. Earth Sci.*, *29*, 257–268, 1999.

Mortimer, N., F. Davey, A. Melhuish, J. Yu, and N. J. Godfrey, Geological interpretation of a deep seismic reflection profile across the Eastern Province and Median Batholith, New Zealand: Crustal architecture of an extended Phanerozoic convergent margin, *N. Z. J. Geol. Geophys.*, in press, 2002.

Norris, R. J., and A. F. Cooper, Late Quaternary slip rates and slip partitioning on the Alpine Fault, New Zealand, *J. Struct. Geol.*, *23*, 507–520, 2000.

Norris, R. J., P. O. Koons, and A. F. Cooper, The obliquely-convergent plate boundary in the South Island of New Zealand: Implications for ancient collision zones, *J. Struct. Geol.*, *12*, 715–725, 1990.

O'Connell, R. J., and B. Budiansky, Seismic velocities in dry and saturated cracked solids, *J. Geophys. Res.*, *79*, 5412–5426, 1974.

Okaya, D., and S. Henrys, Pre-stack Kirchoff migration of the CDP98 Data: Do we have reflections from the Alpine fault zone?, South Island Workshop Report, Univ. of South. Calif., Los Angeles, 1999.

Okaya, D., N. Christensen, D. Stanley, and T. Stern, Crustal anisotropy in the vicinity of the Alpine fault zone, *N. Z. J. Geol. Geophys.*, *38*, 579–583, 1995.

Okaya, D. A., S. Henrys, and T. A. Stern, "Super-gathers" across the South Island of New Zealand: Double-sided onshore-offshore seismic imaging of a plate boundary, *Tectonophysics*, in press, 2002.

Parker, P. B., Genetic algorithms and their use in geophysical problems, Ph.D. thesis, 202 pp., Univ. of Calif., Berkeley, 1999.

Pysklywec, R. N., C. Beaumont, and P. Fullsack, Lithospheric deformation during the early stages of continental collision: Numerical experiments and comparison with South Island, New Zealand, *J. Geophys. Res.*, *107*(B7), 2133, 10.1029/2001JB000252, 2002.

Reyners, M., Subcrustal earthquakes in the central South Island, New Zealand, and the root of the Southern Alps, *Geology*, *15*, 1168–1171, 1987.

Scherwath, M., T. Stern, and S. Henrys, Model of onshore-offshore data along Southern Alps Transect II, paper presented at New Zealand Geophysical Society Annual Meeting, Wellington, New Zealand, 2000.

Shi, Y., R. Allis, and F. Davey, Thermal modelling of the Southern Alps New Zealand, *Pure Appl. Geophys.*, *146*, 469–501, 1996.

Smith, E. C. G., T. Stern, and B. O'Brien, A seismic velocity profile across the central South Island from explosion data, *N. Z. J. Geol. Geophys.*, *38*, 565–570, 1995.

Stern, T. A., P. E. Wannamaker, D. Eberhart-Phillips, D. Okaya, F. J. Davey, and S. I. P. W. Group, Mountain building and active deformation studied in New Zealand, *Eos Trans. AGU*, *78*, 329, 335–336, 1997.

Stern, T., P. Molnar, D. Okaya, and D. Eberhart-Phillips, Teleseismic *P* wave delays and modes of shortening the mantle lithosphere beneath South Island, New Zealand, *J. Geophys. Res.*, *105*, 21,615–21,631, 2000.

Stern, T., S. Kleffmann, D. Okaya, M. Scherwath, and S. Bannister, Low seismic-wave speeds and enhanced fluid pressure beneath the Southern Alps of New Zealand, *Geology*, *29*, 679–682, 2001.

Sutherland, R., F. Davey, and J. Beavan, Plate boundary deformation in South Island, New Zealand, is related to inherited lithospheric structure, *Earth Planet. Sci. Lett.*, *177*, 141–151, 2000.

Thurber, C. H., Earth structure and earthquake locations in the Coyote Lake area, central California, Ph.D. thesis, Mass. Inst. of Technol., Cambridge, 1981.

Thurber, C. H., Earthquake locations and three-dimensional crustal structure in the Coyote Lake area, central California, *J. Geophys. Res.*, *88*, 8226–8236, 1983.

Thurber, C. H., Local earthquake tomography: Velocities and *Vp/Vs*—Theory, in *Seismic Tomography: Theory and Practice*, edited by H. M. Iyer and K. Hirahara, pp. 563–583, Chapman and Hall, New York, 1993.

Thurber, C., and D. Eberhart-Phillips, Local earthquake tomography with flexible gridding, *Comput. Geosci.*, *25*, 809–818, 1999.

Thurber, C., S. Roecker, W. Ellsworth, Y. Chen, W. Lutter, and R. Sessions, Two-dimensional seismic image of the San Andreas fault in the northern Gabilan Range, central California: Evidence for fluids in the fault zone, *Geophys. Res. Lett.*, *24*, 1591–1594, 1997.

Todd, T., and G. Simmons, Effect of pore pressure on the velocity of compressional waves in low-porosity rocks, *J. Geophys. Res.*, *77*, 3731–3743, 1972.

Toksoz, M. N., C. H. Cheng, and A. Timur, Velocities of seismic waves in porous rocks, *Geophysics*, *41*, 621–645, 1976.

Toomey, D. R., and G. R. Foulger, Tomographic inversion of local earthquake data from the Hengill-Grensdalur central volcano complex, *Iceland, J. Geophys. Res.*, *94*, 17,497–17,510, 1989.

Tullis, J., R. Yund, and J. Farver, Deformation-enhanced fluid distribution in feldspar aggregates and implications for ductile shear zones, *Geology*, *24*, 63–66, 1996.

Upton, P., T. G. Caldwell, C. P. Chamberlain, D. Craw, Z. James, G. J. Jiracek, P. O. Koons, and P. E. Wannamaker, Fluids in a backthrust regime, Southern Alps, New Zealand, *J. Geochem. Explor.*, *69–70*, 517–521, 2000.

Van Avendonk, H. J., W. S. Holbrook, J. K. Austin, D. Okaya, and S. I. P. W. Group, Seismic velocity and wide-angle reflectivity structure of the Australian-Pacific plate boundary, South Island, New Zealand, *Eos Trans. AGU*, *80*(46), Fall Meet. Suppl., F1029, 1999.

Walcott, R. I., Modes of oblique compression: Late Cenozoic tectonics of the South Island of New Zealand, *Rev. Geophys.*, *36*, 1–26, 1998.

Wang, C.-Y., W. Lin, and F. T. Wu, Constitution of the San Andreas fault zone at depth, *Geophys. Res. Lett.*, *5*, 741–744, 1978.

Wannamaker, P. E., G. R. Jiracek, J. A. Stodt, T. G. Caldwell, V. M. Gonzalez, J. D. McKnight, and A. D. Porter, Fluid generation and pathways beneath an active compression orogen, the New Zealand Southern Alps, inferred from magnetotelluric data, *J. Geophys. Res.*, *107*(B6), 2117, 10.1029/2001JB000186, 2002.

Wessel, P., and W. H. F. Smith, New version of the generic mapping tools released, *Eos Trans. AGU*, *79*, 579, 1998.

Wilson, D., and D. Eberhart-Phillips, Estimating crustal thickness in the central South Island, *Sci. Rep. 98/27*, Inst. of Geol. and Nucl. Sci., Lower Hutt, 1998.

Winkler, K. W., and W. F. I. Murphy, Acoustic velocity and attenuation in porous rocks, in *Rock Physics and Phase Relations: A Handbook of Physical Constants*, edited by T. J. Ahrens, pp. 20–34, AGU, Washington, D. C., 1995.

Wood, P. R., and J. G. Begg, Waitaki hydroelectric development: Identification of active faults, *Client Rep. 90/11*, N. Z. Geol. Surv., Lower Hutt, 1990.

Woodward, D., The crustal structure of the Southern Alps, New Zealand, as determined by gravity, *Bull. R. Soc. N. Z.*, *18*, 95–98, 1979.

—————————

D. Eberhart-Phillips, Institute of Geological and Nuclear Sciences, Private Bag 1930, Dunedin, New Zealand. (D.Eberhart-Phillips@gns.cri.nz)

S. Bannister, Institute of Geological and Nuclear Sciences, POB 30368, Lower Hutt, New Zealand. (s.bannister@gns.cri.nz)
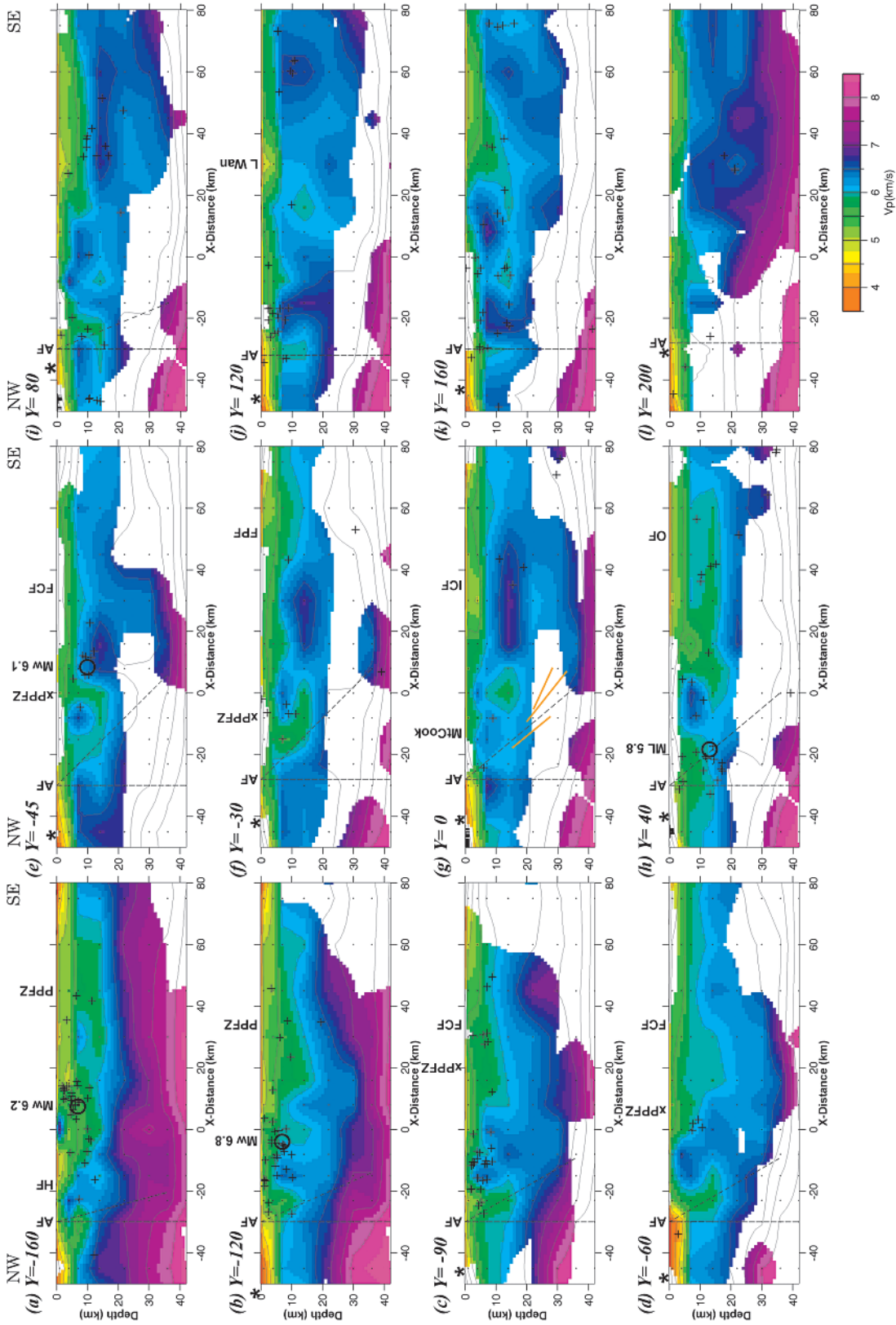
**Figure 8.** Y cross sections of *Vp* model. Areas with low resolution (DRE < 5) are masked but contoured. Each section shows hypocenters (pluses) midway to next section. Small dots indicate velocity nodes. Stars at the top of sections denote the coastline. Dip of Alpine fault is not known, so both vertical and dipping lines are shown. Locations are indicated for the Alpine fault (AF), Hope fault (HF), Porters Pass fault zone (PPFZ) and incipient PPFZ (xPPFZ), Forest Creek fault (FCF), Fox Peak fault (FPF), Mt. Cook, Irishman's Creek fault (ICF), Ostler fault (OF), Lake Wanaka. Reflectors from CDP line [*Okaya and Henrys*,1999] are shown in orange in Figure 8g. Circles show significant earthquakes.
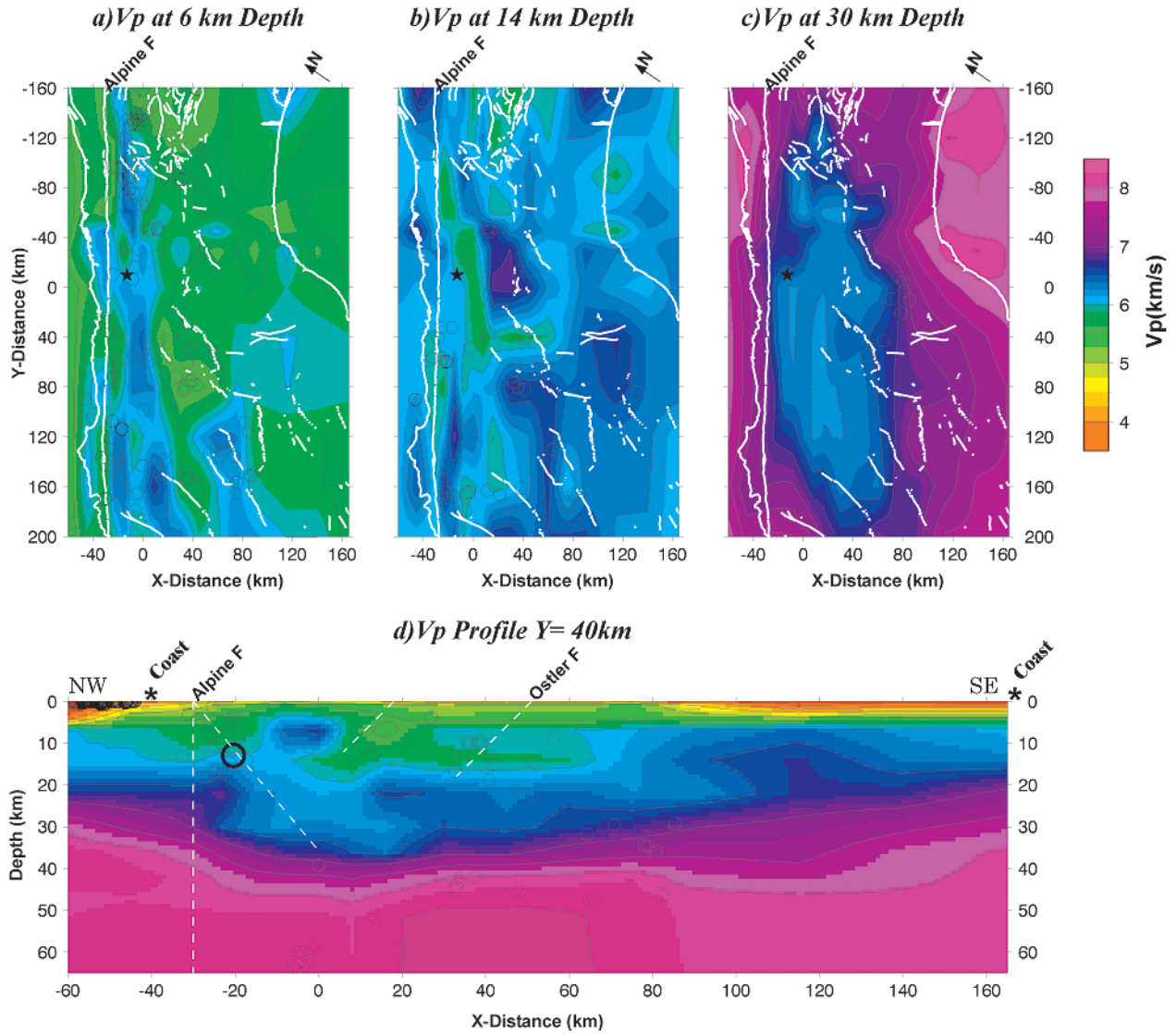
**Figure 11.** Map-views of 3-D *Vp* model at (a) 6-km depth, hypocenters 2.5 to 10.5 km depth, (b) 14-km depth, hypocenters 10.5 to 22 km depth, (c) 30-km depth, hypocenters 22 to 36 km depth; star indicates Mt. Cook. (d) $y = 40$ cross section to 65-km depth; hypocenters from $y = 0$ to 80 km are shown as circles, including the 1998 $M_L$ 5.8 in bold; simplified faults in white; compare to Figure 2.